



**HAL**  
open science

## A testing technique for concrete under confinement at high rates of strain

P. Forquin, G. Gary, F. Gatuingt

### ► To cite this version:

P. Forquin, G. Gary, F. Gatuingt. A testing technique for concrete under confinement at high rates of strain. *International Journal of Impact Engineering*, 2008, 35 (6), pp.425. 10.1016/j.ijimpeng.2007.04.007 . hal-00499102

**HAL Id: hal-00499102**

**<https://hal.science/hal-00499102>**

Submitted on 9 Jul 2010

**HAL** is a multi-disciplinary open access archive for the deposit and dissemination of scientific research documents, whether they are published or not. The documents may come from teaching and research institutions in France or abroad, or from public or private research centers.

L'archive ouverte pluridisciplinaire **HAL**, est destinée au dépôt et à la diffusion de documents scientifiques de niveau recherche, publiés ou non, émanant des établissements d'enseignement et de recherche français ou étrangers, des laboratoires publics ou privés.

## Author's Accepted Manuscript

A testing technique for concrete under confinement  
at high rates of strain

P. Forquin, G. Gary, F. Gatuingt

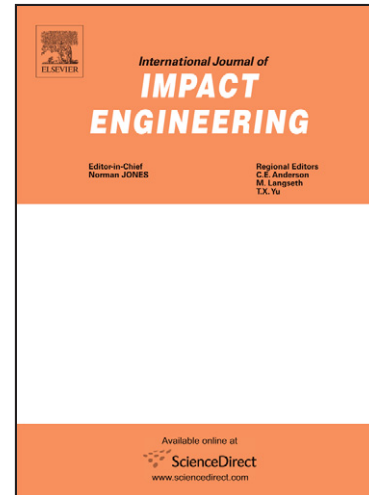
PII: S0734-743X(07)00067-X  
DOI: doi:10.1016/j.ijimpeng.2007.04.007  
Reference: IE 1483

To appear in: *International Journal of Impact*

Accepted date: 25 April 2007

Cite this article as: P. Forquin, G. Gary and F. Gatuingt, A testing technique for concrete under confinement at high rates of strain, *International Journal of Impact* (2007), doi:10.1016/j.ijimpeng.2007.04.007

This is a PDF file of an unedited manuscript that has been accepted for publication. As a service to our customers we are providing this early version of the manuscript. The manuscript will undergo copyediting, typesetting, and review of the resulting galley proof before it is published in its final citable form. Please note that during the production process errors may be discovered which could affect the content, and all legal disclaimers that apply to the journal pertain.



[www.elsevier.com/locate/ijimpeng](http://www.elsevier.com/locate/ijimpeng)

## A testing technique for concrete under confinement at high rates of strain

P. Forquin<sup>1,\*</sup>, G. Gary<sup>2</sup> & F. Gatuingt<sup>3</sup>

<sup>1</sup> Laboratoire de Physique et de Mécanique des matériaux, Université de Metz, 57045 Metz, France

[Pascal.Forquin@univ-metz.fr](mailto:Pascal.Forquin@univ-metz.fr)

<sup>2</sup> Laboratoire de Mécanique des Solides, Ecole Polytechnique, 91128 Palaiseau, France

[Gary@lms.polytechnique.fr](mailto:Gary@lms.polytechnique.fr) - <http://lmsX.polytechnique.fr/LMSX/>

<sup>3</sup> Laboratoire de Mécanique et Technologie, E.N.S. de Cachan, 94235 Cachan, France

[Fabrice.Gatuingt@lmt.ens-cachan.fr](mailto:Fabrice.Gatuingt@lmt.ens-cachan.fr)

**Abstract:** A testing device is presented for the experimental study of dynamic compaction of concrete under high strain-rates. The specimen is confined in a metallic ring and loaded by means of a hard steel Hopkinson pressure bar (80 mm diameter, 6 m long) allowing for the testing of specimens large enough regarding the aggregates size. The constitutive law for the metal of the ring being known, transverse gauges glued on its lateral surface allow for the measurement of the confining pressure. The hydrostatic and the deviatoric response of the specimen can then be computed. The proposed method is validated by several numerical simulations of tests involving a set of 4 different concrete-like behaviours and different friction coefficients between the cell and the specimen. Finally, 3 tests performed with the MB50 concrete at 3 different strain rates are processed with the method and are compared with literature results for the same material under quasi-static loadings.

**Keywords:** 1D-strain compression test, Hopkinson pressure bar, Deviatoric strength and compaction law, High-performance concrete.

## 1. Introduction

Compaction of concrete with a volume decrease of 10% or more occurs under high pressures. Such situations are found in military applications or in studies connected with the safety of buildings (power plants) regarding an accidental internal loading or external loading (plane crash).

On the one hand, the stress needed for compaction is high (around 1000 MPa) with a large pressure component. On the other hand, the specimens must be large enough to be representative with respect to the size of aggregates. Consequently, the forces required are so large that only a few testing procedures are available in this field. In the quasi-static load regime multiaxial tests use compression cells that are able to support very high pressures [1, 2]. Dynamic plate impact tests are also used [3], for which the strain-rates obtainable are in the range of  $10^5 \text{ s}^{-1}$  or greater.

The testing device presented in this paper is a method of obtaining results between quasi-static and high speed loading rates (from 200 to 2000  $\text{s}^{-1}$ ) where only a few results involving compaction are found.

In this range of loading pressures, the behaviour of concrete is generally described by means of plasticity theories where the hydrostatic and the deviatoric responses are considered separately. The major differences between different models are found in the way both responses are coupled.

---

\* Corresponding author. Tel.: +33-3-87-54-72-49; fax: +33-3-87-31-53-66; email address: forquin@univ-metz.fr

A clear understanding has then to be based on well-defined loading paths. As real loading situations leading to compaction are generally dynamic ones, the study of strain rate effects is important.

A significant literature exists on rate the sensitivity of rock tested at medium strain rates, for example in ancient papers [4, 5], and a more recent one [6]. The early tests on concrete under dynamic loading were performed with pendulum and drop weight tests. An arrangement using impulse loading of a cylindrical specimen made of concrete was used by Goldsmith and co-workers [7] to study the tensile fracture feature of concrete. The use of the compressive Split Hopkinson Pressure Bar (SHPB) to determine the rate sensitivity of concrete can be found in recent works [8-12]. However, the test analysis must consider both material and geometric aspects. For example, the increase of the stress with the strain rate can be due to the radial confinement induced by inertia and/or by the intrinsic rate sensitivity of the material. Indeed, for a material with a non-zero Poisson's ratio, the lateral expansion associated with the compression is restrained by inertia effects [13, 14, 15, 16]. As rock-like materials are very sensitive to the lateral pressure when they are axially loaded, they can show geometry dependent strain-rate sensitivity. In the present case, the confinement cell considerably reduces the radial displacement so the radial pressure induced by inertia does not act.

Dynamic axial compression testing with lateral pressure is not very common. For lower lateral pressures, experimental data have been obtained using a SHPB axial loading system combined with a pressure cell [5, 12, 17, 18]. This technique does not produce the high pressures required for compaction.

A new testing device has been designed and studied by Burlion et al. [2] for the case of quasi-static loading, involving axial and lateral stresses in the range of expected dynamic values. In the

present work, an attempt was made to extend this technique to the dynamic range using a SHPB to produce axial loading and to measure axial forces and displacements. Following a few authors [12, 17, 19], we then propose a test where the specimen is confined in an instrumented metallic ring and loaded by means of a Hopkinson pressure bar (SHPB) especially designed for this purpose.

## 2. General description of the confining compression test

### *Specimen and Cell geometry*

The general idea of the test is described in figure 1. A cylindrical specimen embedded in a steel confinement ring is compressed using 2 cylindrical plugs (Fig. 1a). The concrete specimen has a diameter of 30 mm and is 40 mm long. The steel plugs have the same diameter and a thickness of 10 mm. The steel ring has an outer diameter of 65 mm and is 45 mm long.

### *The “MB50” concrete*

The selected high strength concrete “MB50” has already been extensively studied [20, 21, 22, 23]. The specimens to be tested were machined in a concrete block after being dried (40 days) to prevent the effects of drying shrinkage of the concrete. The composition and the mean mechanical properties of MB50 are detailed in table 1.

*Interface product between the specimen and the cell*

A gap, about 0.2 mm thick, is left between the concrete specimen and the ring. It is filled with an epoxy resin, coated with Teflon. This material is highly incompressible and hence does not reduce the confinement pressure. It also has a weak shear strength allowing for easier relative displacements between the ring and the specimen.

*Direct strain measurements on the cell*

Three hoop strain gauges were glued onto the external surface of the metallic ring. Their outputs allow the deduction of the radial stress and strain within the specimen. One gauge is located in the middle of the ring (n°2), as shown in figure 1b and the two others (n°1 and 3) are located at a distance from the middle equal to  $\frac{3}{4}$  of the half-length of the ring. Three axial gauges (n°4, 5, 6) are located on the same axial planes (Fig. 1b). From their outputs, it is expected to deduce the friction force between the specimen and the ring and to quantify the barrelling of the ring.

*Brief description of the test*

The cell and its plugs are inserted between the two Hopkinson bars. The loading produces compression of the concrete and a subsequent increase of the internal pressure supported by the cylindrical cell. The signals recorded on the two Hopkinson bar gauges allow for the computation of the axial forces and of the corresponding displacements. The signals recorded with the gauges glued on the cell give information on its response under pressure from the concrete specimen.

### 3. The SHPB loading device

#### *Basic description of the SHPB system*

The SHPB (Split Hopkinson Pressure Bar) system, also called Kolsky's apparatus is a commonly used experimental technique in the study of the constitutive laws of materials at high strain rates. The first use of a long thin bar to measure stresses under impact conditions has been reported in [24]. The experimental set-up with two long bars, widely used today, was pioneered by Kolsky [25].

A typical SHPB testing device is composed of long input (or incident) and output (or transmitter) bars with a short specimen placed between them. With the impact of a projectile (or striker) at the free end of the input bar, a compressive longitudinal "incident" wave  $\varepsilon_I(t)$  is created in the input bar. Once the incident wave reaches the interface between the specimen and the bar, a reflected pulse  $\varepsilon_R(t)$  in the input bar and a transmitted pulse  $\varepsilon_T(t)$  in the output bar are developed. With the gauges that are glued on the input and output bars (named A and B, respectively), these three basic waves are recorded. Their processing allows for the knowledge of forces and particle velocities at both faces of the specimen [25].

#### *Recall of the processing technique*

As both the incident and the reflected waves have to be known, the optimal position of a single

gauge station “A” that allows for the longest loading time is the middle of the input bar. The maximum theoretical length of the striker is then half the length of the input bar. In fact, because of the non-zero rising time of the incident wave, the length of the striker has more often to be around 80% of the theoretical one.

The forces and the particle velocities at the specimen faces are calculated with waves shifted to the same points. For slender elastic bars, it is assumed that the elastic waves propagate without dispersion so that they are simply time shifted to the bar ends.

Let us call  $\varepsilon_i(t)$ ,  $\varepsilon_r(t)$  and  $\varepsilon_t(t)$  the corresponding (shifted) waves. For the sake of simplicity, a one-dimensional analysis gives the usual relations between jumps of stress ( $\Delta\sigma$ ), particle velocity ( $\Delta v$ ) and strain ( $\Delta\varepsilon$ ) [26], when a single direction of propagation is considered.

$$\Delta\sigma = \pm\rho c\Delta v, \quad (1a)$$

and, in the 1-D purely elastic case

$$\Delta\varepsilon = \pm\Delta v/c \quad (1b)$$

where  $c$  is the bar wave speed ( $c = (E/\rho)^{1/2}$ ) of a 1-D wave propagating in the bars. Using these equations together with the superposition principle, the velocities and the forces at both specimen faces are given by the following formulas (2a and 2b).

$$\begin{aligned} V_{in}(t) &= -c(\varepsilon_i(t) - \varepsilon_r(t)) \\ V_{out}(t) &= -c\varepsilon_t(t) \end{aligned}, \quad (2a)$$

$$\begin{aligned} F_{in}(t) &= S_b E(\varepsilon_i(t) + \varepsilon_r(t)) \\ F_{out}(t) &= S_b E\varepsilon_t(t) \end{aligned}, \quad (2b)$$

where  $V$  is the velocity,  $F$  the force,  $S_b$  the area of the bars,  $E$  the Young's modulus of the bars. Subscripts *in* and *out* indicate the input and output sides, respectively.

#### *Present SHPB device and processing technique*

The SHPB set-up (striker, input bar and transmitter bar) used here is made of steel bars (elastic limit 1200 MPa) with a diameter of 80 mm. The striker, the input bar and the output bar are 2.2m, 6m and 4 m long, respectively. The strains at points A (middle of input bar) and B (1 m away from the specimen) are measured with strain gauges. Considering the elastic response of the bar and assuming a uniaxial state of stress at the gauges stations, an improved measurement of the strain is made by using a complete gauge bridge. At the given position of the gauge station, each couple of transverse and longitudinal gauges are diametrically opposed on the surface of the bar to eliminate a possible bending component of the strain. The transverse strain is equal to the longitudinal strain multiplied by the Poisson's ratio. The gauges that are used are “2mm, Kyowa - KSN-2-120-F3-11” type. The bridge is supplied by a monitored 8 Volts supply and the signals are amplified (amplifier gain 100-200-500-1000, six channels, bandwidth 200 kHz). They are then recorded with a data acquisition card (12 bits) with the time base set to the value of 1  $\mu$ s. Knowing that the wave speed is equal to 5120 m/s, it can be simply deduced from the dimensions of the set up that the loading pulse duration is equal to 860  $\mu$ s. The beginning of the reflected wave arises 300  $\mu$ s later than the end of the incident pulse. Both waves are thus easily separated (Fig. 2).

The shifting of the waves to the specimen ends takes account of dispersion. We use a dispersion relation that is the first mode solution of the Pochhammer [27] and Chree [28]

equation, computed for the material constants of our bars. Since the bars have an unusually large diameter, it is worth checking that only the first mode is involved. A spectral analysis of the gauge signals recorded shows a negligible amplitude for frequencies greater than 20 kHz. The cut-off frequency of the second mode is, in the case of our bars, close to the same value (from Davies [29] it is known that the minimum phase velocity for the second mode corresponds to  $a/\Lambda = 0.25$  and the minimum group velocity corresponds to  $a/\Lambda = 0.3$  where  $a$  is the radius of the bar and  $\Lambda$  the wavelength. Here,  $a$  and  $c$  (equation 1) are equal to 0.04 m and 5120 m/s respectively. The corresponding cut-off frequencies are equal to 32 kHz and 38.4 kHz respectively). An easy check of the quality of the dispersion correction can be performed by the long distance travel of a wave using the input bar with both free ends after the loading (as shown in [30, 31]).

It was also checked that below 20 kHz, the proportionality of lateral and longitudinal strain is true to better than 99% (from Tyas and Watson [32]) taking account of the energy spectrum of our waves. A complete bridge involving lateral and axial strains can then be safely used for this measurement.

For precise time shifting, an assisted delay setting method was used. This is based on the existence of an initial elastic response of the specimen. During the corresponding time, real reflected and transmitted waves are compared with theoretical ones computed from the knowledge of the incident wave and an assumed elastic behaviour of the specimen [33, 30]. This data processing method ensures precise measurements at low strains (in the range of strains lower than 1%) [11].

Using equations (2), the forces and the velocities (and the displacements, by integration) at both sides of the complete specimen (including the plugs) are calculated. These data are the

results of a one-dimensional analysis. The force is the integral of the axial stress over the specimen area while the velocity is the mean velocity of the bar end.

*The compression device used for dynamic testing*

The device used for dynamic testing was briefly described in figure 1. The complete cell composed of the specimen, the steel ring and the plugs is inserted between two Hopkinson bars. It would have been easier to use a cell with the same inner diameter as bars and avoid the use of plugs. However, to produce the expected axial stress level (evaluated from quasi-static test results) of -1000 MPa, the value of the striker speed of a steel SHPB needed in this case should have been 50 m/s. We have experienced that such a striker speed induces the unsticking of the strain gauges and for this reason it is necessary to keep the striker speed under 20 m/s. A reduction of area between the specimen and the bar is therefore necessary. This explains the design dimensions of the bars and of the specimen and the use of steel plugs.

The elastic limit of the plugs is higher than the maximum stress obtained in our tests and the elastic shortening of the plugs can easily be subtracted from the total shortening measured.

For a more precise correction, a test with the two plugs alone was performed within the range of the maximum force observed in tests with the complete device. From the corresponding relation between the force and the displacement, a lower Young's modulus than that for steel was found. The reason is that the total average displacement (regarding the section of the bar) is the sum of the elastic compression of the plugs and the local elastic punching of bar ends. This needs to be subtracted from the displacement measured in the tests with the complete device.

## **4. A method to measure states of stress and strain during confined 1D-strain compression tests**

At high stress levels, a high axial strain and rather small (but not negligible) radial strain of the specimen are observed. In order to evaluate the compaction law of the concrete, an accurate measurement of the state of stress and strain within the specimen is needed. For this, one first needs to know the elastic (and possibly elastoplastic) behaviour of the material of the ring. The identification of the mechanical behaviour of this material is presented in subsection 4.2.

The complete method used to compute the mechanical behaviour of the sample is explained in subsection 4.3. With this method, the state of strain and stress is measured knowing, on the one hand, the axial forces and displacements at the specimen end surfaces and, on the other hand, the outer strain of the ring. The lateral pressure between the ring and the specimen is deduced from the strains measured on the ring and is corrected for the real length of the specimen. The axial stress is computed from the axial forces taking into account the (small) lateral expansion - the radial strain - of the specimen.

Several numerical simulations were performed and are presented in subsection 4.4 with different sets of parameters for the Krieg, Swenson and Taylor model with 2 friction coefficients to validate the method and its robustness. In the section 5, this method is applied to three 1-D-strain compression tests.

#### 4.1. BASIC ANALYSIS

Considering that the cell is elastic and that its cylindrical shape is undeformed (that means that a possible barrelling effect is neglected), a basic analysis of the test can be done. The hoop external strain ( $\varepsilon_{\theta\theta}^{ext}$ ) and the internal pressure ( $P_{int}$ ) are related in the following way (formula valid for an infinite cylinder):

$$\varepsilon_{\theta\theta}^{ext} = \frac{P_{int}}{E_c} \frac{2R_i^2}{(R_e^2 - R_i^2)}, \quad (3)$$

where  $E_c$ ,  $R_i$ ,  $R_e$  are the Young's modulus of the cell and the inside and outside radius of the cell, respectively.

The length of the specimen will vary during the test, so that friction forces will appear between the specimen and the cell. These forces will contribute to the overall compression force measured by the SHPB. They also should induce an axial strain in the cell. Assuming a state of equilibrium of the cell and a constant friction force, the loading can be described with two opposite and symmetric homogeneous axial forces acting along the internal diameter of the cell. The subsequent axial strain within the steel ring will decrease (in absolute value) from the middle, where its value is equal to  $\varepsilon_{axial}^{max}|_{fr}$ , to zero at the specimen ends. In that case, one has:

$$\varepsilon_{axial}^{max}|_{fr} = \frac{1}{E_c} f P_{int} R_i H / (R_e^2 - R_i^2), \quad (4)$$

where  $H$  is the height of the cell and  $f$  the friction coefficient.

Following this elementary analysis, the internal pressure and the friction forces could then be

measured and the axial stress could be calculated from the global force and from the friction forces. The main difficulty with this analysis is that it needs a cell thin enough to provide measurable strains (due to friction) but also a cell thick enough to prevent barrelling. It is shown in the following that both requirements cannot be met and that the processing of the strain data measured on the cell must be more sophisticated.

#### **4.2. IDENTIFICATION OF THE BEHAVIOR OF THE STEEL OF THE CELL**

The behaviour of the steel used for the ring component was identified by means of two dynamic compression tests performed at strain rates of approximately  $200 \text{ s}^{-1}$  and  $300 \text{ s}^{-1}$ . The strong strain hardening and the high failure strain observed (Fig. 3) allow avoiding any strain localisation within the steel ring. The plastic behaviour of the steel is described by a piece-wise linear law (Fig. 3). It is assumed to be the same for any part of the cell. The Young's modulus is taken equal to  $2 \times 10^5 \text{ MPa}$ .

#### **4.3. NUMERICAL ANALYSIS OF THE RESPONSE OF THE CELL FOR THE TEST ANALYSIS**

In order to analyse the response of the cell submitted to internal pressure and friction forces numerical simulations were undertaken. They take account of the variable axial length where the pressure is applied (simulating the change of the specimen length during the loading) and of the elastoplastic behaviour of the cell.

#### 4.3.1 Strains induced by a uniform pressure applied to the inner surface of the cell

First, it was determined how the pressure applied by the concrete to the inner surface of the cell is related to the hoop strain measured at its outer surface. To do so, numerical simulations of the cell loaded by an internal pressure were carried out using the finite element computer code Abaqus Implicit [34]. A similar approach had previously been successfully applied to a smaller steel ring whose elastic limit was lower [35]. The computations showed a noticeable barrelling of the cell. In the present case, the geometry of the cell was as described before (outer diameter 65 mm, inner diameter 30 mm and height 45 mm). Two numerical simulations were carried out to take account of the change in length of the specimen during the test. In both cases, a radial compressive stress was applied to the inner surface (cylindrical). In the first case, this pressure was applied to a central part of the cell 40 mm long (smaller than the cell length), equal to the initial length of the sample. In the second numerical simulation, the pressure was applied to a shorter central part 34 mm long (equal to the specimen length at the end of the test in the case of a nominal axial strain equal to -15%). This value is close to the ultimate level of strain that is reached during the tests. The two curves (internal-radial-stress versus external-hoop-strain) are plotted in figure 4. A linear interpolation between these 2 results is used to take account of the real length of the sample during the test. The length of the specimen is directly deduced from SHPB data.

From both simulations, it was shown that the cell remains in the elastic range when the internal pressure is lower than approximately 300 MPa, and the external hoop strain is approximately lower than 0.1%. Anyway, the post-processing of the data proposed below, based on the interpolation between the above loadings, is still possible when the cell is plastically

loaded. In such a case, the same cell could not be used more than once.

The radial inner stress  $\bar{\sigma}_{radial}^{(int)}$  is related to the measured outer hoop strain  $\varepsilon_{\theta\theta}^{(z=0, ext)}$  in the following way:

$$-\bar{\sigma}_{radial}^{(int)}(\bar{\varepsilon}_{axial}, \varepsilon_{\theta\theta}^{(z=0, ext)}) = \left(1 - \frac{\bar{\varepsilon}_{axial}}{\varepsilon_B}\right) \sigma_A(\varepsilon_{\theta\theta}^{(z=0, ext)}) + \left(\frac{\bar{\varepsilon}_{axial}}{\varepsilon_B}\right) \sigma_B(\varepsilon_{\theta\theta}^{(z=0, ext)}), \quad (5)$$

where  $\sigma_A$  and  $\sigma_B$  are the functions identified from figure 4, associated with a null strain (specimen length 40 mm) and a strain  $\varepsilon_B$  equal to 0.15 (specimen length 34 mm), respectively. It will be assumed in the following that the radial stress is homogeneous in the sample and consequently is equal to the radial stress applied by the sample to the cell ( $\bar{\sigma}_{radial}^{(int)} = \bar{\sigma}_{rr}^S$ ).

Moreover, in the above simulations, the strains (and stresses) can be calculated at any point in the cell. Fig. 5 shows the evolution of the inner hoop strain at points ( $z = 0$ , the axial symmetry plane and  $z = h_0/2$ , the initial specimen ends) for both simulated loading cases (A and B) as a function of the external hoop strain ( $\varepsilon_{\theta\theta}^{(z=0, ext)}$ ). It appears (as expected) that the barrelling effect is stronger in case B ( $h_{press} = 34$  mm) than in case A ( $h_{press} = 40$  mm).

It is then possible to compute the average inner hoop strain along the specimen height (between  $z = 0$  to  $z = h_{specimen}/2$ ) knowing the outer hoop strains measured on the cell and the axial strain of the specimen. The average radial strain of the specimen being known, the average specimen area may be also computed as a function of the outer hoop strain ( $\varepsilon_{\theta\theta}^{(z=0, ext)}$ ):

$$\bar{A}_s = A_0(1 + f(\varepsilon_{\theta\theta}^{(z=0, ext)}))$$

The average axial stress is then:

$$\overline{\sigma_{zz}^s} = \frac{F_{axial}}{A_s}, \quad (6)$$

This value  $F_{axial}$  is not directly computable by the SHPB analysis as the force deduced from SHPB measurements also includes the force induced by friction mechanisms. In order to evaluate the importance of the corresponding friction force, new simulations were made: the cell is loaded with a uniform shear stress combined with the uniform pressure previously applied to the inner surface.

#### 4.3.2 Effect of a uniform shear stress applied to the inner surface of the cell in addition to the internal pressure

The above simulations confirm that the internal pressure induces a barrelling of the ring. Friction between the specimen and the ring would also induce barrelling. It is thus important to check how such friction could modify the value of the external hoop strain from which the internal pressure is calculated. Furthermore, as explained in subsection 4.1, the friction forces would induce an overestimation of the axial stress in the specimen if the stress level was directly deduced from the axial force given by standard SHPB analysis.

So, in the simulation, shear stresses were applied, in addition to the internal pressure. These shear stresses were set to be equal to 10% of the normal stress (corresponding to a friction coefficient equal to 0.1). They are imposed via nodal forces (for reasons of convenience) in the direction  $-z$  (for  $z > 0$ ), so the direction of these nodal forces does not change with the cell deformation. The result of one simulation (with shear) is illustrated in figure 6 showing the evolution of the internal pressure according to the outer hoop strain (a slope of pressure from 0 to

800 MPa and shear stress from 0 to -80 MPa were applied over a height  $h_{press}$  of 40 mm). This curve is compared with the first simulation without friction previously presented in figure 4.

It is observed that, for the same outer hoop strain, the radial stress is decreased by 3 to 5% when friction is added to the internal pressure. Neglecting the friction would then lead to a slightly overestimated internal pressure deduced from the external hoop strain. It is explained, in other words, by the fact that the barrelling of the cell, and consequently the external hoop strain, is increased by the shear at a given pressure.

As it is planned to measure the friction from the axial strain at the outer surface, figure 7 shows a comparison of the ratio between the external axial strain and the hoop strain at the measuring middle point ( $z = 0$ ) with and without friction, for a height of the loaded area equal to 34 and 40 mm. The results are plotted as a function of the internal pressure increasing from 0 to 600 MPa (the pressure range observed during the tests will be given latter). The axial strain at measuring points n°4 or n°6 ( $z = 3H/8$ ) appears very small. Consequently, it was not used in the data processing.

The external axial strain appears to be much more influenced by the height of the loaded area than by the amplitude of the friction, so that it seems difficult to evaluate friction from the outer axial strain of the cell. However, figure 7 shows some indications about how the friction might be evaluated from the axial strain. For example, if the internal pressure was lower than 300 MPa (elastic deformation of the cell) and if a small axial strain of the specimen was considered ( $h_{press} = 40$  mm), the outer axial strain would appear negative without friction or positive if friction forces were acting. In fact, a negative axial strain is the consequence of the uniaxial stress state that exists close to the outer surface of the specimen (because  $\sigma_{\theta\theta} > 0$ ,  $\sigma_{zz} \approx \sigma_{rr} \approx 0$ ) whereas a positive axial strain is the result of the barrelling deformation due to friction. In contrast to the

simple analytical solution (equation 4), friction is seen to induce a positive increment of axial strain.

The same figure shows that, if an internal pressure higher than 300 MPa is considered, the axial strain level is strongly influenced by the height of the loaded area and weakly by the magnitude of the friction. In this case, the ratio between the measured hoop strains at points 1 and 2 appears more reliable (figure 8).

The ratio between the hoop strains measured ( $\varepsilon_{\theta\theta}^{(z=3H/8, ext)} / \varepsilon_{\theta\theta}^{(z=0, ext)}$ ) is as much influenced by the friction as by the internal height of the loaded area (figure 8). Nevertheless, the level of the remote hoop strain is much higher than that of the axial strain and the sensitiveness of the measure is increased. If the internal pressure is less than 300 MPa (elastic deformation of the cell) and if the axial strain of the specimen is lower than a few percents ( $h_{press} = 40$  mm), the ratio of hoop strains will be equal to 0.84 without friction and to 0.76 with friction. It corresponds to a decrease of 9% due to friction. If the internal pressure is equal to 600 MPa, the ratio of hoop strains decreases to 0.70 ( $h_{press} = 40$  mm) or 0.57 ( $h_{press} = 34$  mm). So, knowing the internal pressure applied and the axial strain of the specimen, the ratio of hoop strains could be used to evaluate the magnitude of the friction.

These observations show that an extra "barrelling" deformation is generated by a shear stress applied along the inner surface. This deformation leads to an increase of the difference between the outer hoop strains measured ( $\varepsilon_{\theta\theta}^{(z=3H/8, ext)}$ ,  $\varepsilon_{\theta\theta}^{(z=0, ext)}$ ) and an increase of outer axial strain ( $\varepsilon_{zz}^{(z=0, ext)}$ ). Moreover, a friction coefficient of 0.1 between the cell and the sample can induce a slight over-estimation of the inner radial stress (of approximately 4%) and of the inner hoop strain (of approximately 6%) not detailed above.

#### 4.3.3 Evaluation of the possible influence of friction forces (added to the force resulting from pure axial stresses) on the computed specimen behaviour

As explained before, the friction leads to an over-estimation of the axial stress. The corresponding maximum relative error can be related to the contact forces:

$$Err(\sigma_{zz}) = \frac{F_{ax}^{fr}}{F_{ax}} = \frac{\pi D \frac{h}{2} f \sigma_{rr}}{\pi \frac{D^2}{4} \sigma_{zz}} = \frac{2h}{D} f \frac{\sigma_{rr}}{\sigma_{zz}}, \quad \text{with} \quad \frac{\sigma_{rr}}{\sigma_{zz}} = \frac{1 - \frac{1}{3} \frac{\sigma_{dev}}{P}}{1 + \frac{2}{3} \frac{\sigma_{dev}}{P}} \quad (7, 8)$$

where  $f$  is the friction coefficient,  $h$  and  $D$  the height and the diameter of the sample respectively.  $\sigma_{rr}$  and  $\sigma_{zz}$ , are the average radial stress and the axial stress in the sample, respectively. So, the corresponding error can be evaluated knowing the geometry of the specimen, the friction coefficient and the ratio between the deviatoric strength and pressure. The smaller this ratio, the higher is the error (equations 7 and 8). The tests that are presented later in the paper show that the ratio ( $\sigma_{dev}/P$ ) always remained above 0.9. Therefore, the maximum ratio between the radial stress level and the axial stress level is approximately 0.44 (equation 8). If the initial dimensions of the specimen are considered ( $h = 40$  mm,  $D = 30$  mm) it appears that the relative error in the axial stress induced by a friction coefficient  $f$  is always under  $1.2f$  (i.e. 12% if  $f = 0.1$ , equation 7). The numerical simulations done with and without friction will give a more precise evaluation of the error that could arise from neglecting the friction.

#### 4.3.4 Computation of the mechanical fields involved in the material behaviour

The radial stress being known, the average deviatoric stress is:

$$\bar{\sigma}_{deviatoric}^S = \left| \bar{\sigma}_{zz}^S - \bar{\sigma}_{rr}^S \right|, \quad (9)$$

the average hydrostatic pressure and the volumetric strain are given by the formulas:

$$\bar{P}_{hydrostatic}^S = -\frac{1}{3}(\bar{\sigma}_{zz}^S + 2\bar{\sigma}_{rr}^S), \quad (10)$$

$$\bar{\varepsilon}_{volumic}^S = (1 + \bar{\varepsilon}_{axial}^S)(1 + \bar{\varepsilon}_{rr}^S)^2 - 1. \quad (11)$$

Knowing the axial stress and the internal pressure, the deviatoric behaviour (i.e. the supposed evolution of the deviatoric stress versus the hydrostatic pressure) and hydrostatic behaviour (variation of the volumetric strain versus the hydrostatic pressure) can be calculated.

#### 4.4. A NUMERICAL VALIDATION OF THE METHOD

In order to check the validity of the proposed method used to process the experimental data, artificial experimental tests were performed using numerical simulations. These simulations use the concrete plasticity model (the KST model, see underneath) with 4 different sets of parameters in order to evaluate a large enough range of possible behaviours. Meanwhile, the main hypothesis introduced in subsection 4.3 will be justified (influence of the specimen shortening, of the cell expansion, and of the friction coefficient).

This material model is not rate-sensitive. In the dynamic range, very small rate sensitivity for the tested concrete will be demonstrated (chapter 5) that validates the present assumption.

##### 4.4.1 The Krieg, Swenson and Taylor (KST) model

The model of Krieg, Swenson and Taylor [36, 37] is relatively simple and was implemented as a Fortran procedure (Vumat) in the Abaqus-explicit code [38]. It describes the hydrostatic behaviour by a compaction law linking the volumetric strain to the hydrostatic pressure (figure 9, right). The final constant bulk modulus  $K_f$  (Table 2) was used for the highest pressures ( $P > 1$  GPa). Moreover, the Von Mises equivalent stress  $\sigma_{eq}$  cannot exceed some function of the hydrostatic pressure  $P$  (equation 12).

$$\sigma_{eq} = \min_p \left( \sqrt{a_0 + a_1 P + a_2 P^2}, \sigma_{mises}^{\max} \right) \quad (12)$$

The coefficients ( $a_0, a_1, a_2$ ) used in the subsequent simulations were identified from triaxial compression tests carried out under different confining pressures with MB50 concrete [23]. These coefficients are given in table 2. The numerical simulations of the 1D-strain compression test were performed with 4 different sets of parameters illustrated in figure 9 (table 2).

#### 4.4.2 Numerical simulations of one 1D-strain compression test

Half of the cylindrical concrete specimen was compressed between a cylindrical steel compression plug and the symmetry plane ( $z = 0$ , figure 10) where a boundary condition of null axial displacement is imposed. An axial velocity is imposed on the upper surface of the compression plug. This dynamic numerical simulation will then account for radial inertia effects. The axial velocity imposed at one face of (half) the specimen is time dependent, in a close way, to the (half) difference of input and output speeds measured with SHPB. It then takes account of axial transient effects in the specimen. Only the axial movements of rigid bodies are neglected.

They are proved to be negligible by the fact that, at the end of the test, the global relative displacement between the specimen and the cell is then than 2 mm. These assumptions follow usual assumptions used to process standard SHPB tests [25]. Under-integrated axi-symmetric finite elements CAX4R were used. The numerical simulation of figure 10 uses parameters given in table 2 (concrete n°1). Figures 10a and 10b show the iso-contours of the axial and hoop strains for a nominal axial strain nearly equal to -20%. One can notice the continuity of the hoop strain field between the sample and the cell. The axial strain and the stress fields are also almost homogeneous in the sample ( $-1100 \text{ MPa} > \sigma_{zz} > -1400 \text{ MPa}$ ). A concentration of stresses is observed near the contact between the plug and the sample. This is due to the smaller diameter of the plug (figure 10d). Moreover, it is observed that the radial stress is homogeneous in the sample and is constant at the contact surface between the plug and the sample (figure 10c). This point reinforces the assumptions used for the numerical simulations involving the cell only (figure 4).

#### 4.4.3 Validation of the processing method by its application to numerically simulated data

The following figures (11 to 13) show the results of the procedure applied to numerical simulations. The loading is applied up to an axial strain of -25%. The left-hand side figures present the deviatoric behaviour (evolution of the deviatoric stress versus the hydrostatic pressure) while the right-hand ones show the hydrostatic behaviour (compaction). As explained in section 4.3, in the processing method, the mean radial stress and the mean strain of the specimen are computed knowing the external hoop strain of the cell and the mean axial strain of the specimen (equation 5); the axial stress is computed as a function of the axial force and the radial strain of the specimen (equation 6). Therefore, the “measured” (i.e. processed) deviatoric

stress ( $\bar{\sigma}_{deviatoric}^{measured}$ ), the “measured” hydrostatic pressure ( $\bar{P}_{hydrostatic}^{measured}$ ) and the “measured” volumetric strain ( $\bar{\epsilon}_{volumic}^{measured}$ ) are deduced from equations 9, 10 and 11 using the variables defined underneath (13, 14 and 15).

$$\bar{\sigma}_{rr}^S(\epsilon_{\theta\theta}^{ext-cell}, \bar{\epsilon}_{axial}^S) \quad (13)$$

$$\bar{\epsilon}_{rr}^S(\epsilon_{\theta\theta}^{ext-cell}, \bar{\epsilon}_{axial}^S) \quad (14)$$

$$\bar{\sigma}_{zz}^S(F_{axial}, \bar{\epsilon}_{rr}^S) \quad (15)$$

Independently of the processing method, a direct knowledge of the specimen/cell contact force ( $F_{radial}$ ) is provided by the numerical simulations. A new mean radial stress may be computed from this contact force and the axial strain of the specimen (defined in 16). This radial stress may be compared, at any time, with the one of the processing method computed with equation 5 (defined in 13).

$$\bar{\sigma}_{rr}^S(F_{radial}, \bar{\epsilon}_{axial}^S) \quad (16)$$

The “contact” deviatoric stress ( $\bar{\sigma}_{deviatoric}^{contact}$ ) and the hydrostatic pressure ( $\bar{P}_{hydrostatic}^{contact}$ ) are deduced from equations 9 and 10 using the variables defined in 15 and 16.

Consequently, for each following graph, three curves are presented: the first curve (A -plain line) corresponds to the imposed material behaviours according to figure 9 (table 2). The second (B -dotted curves with triangles) is obtained with the method proposed in subsection 4.3 that will be used to process experimental data (defined in 13, 14 and 15). The third curve (C -with round

symbols) is plotted using the stresses (defined in 15 and 16) obtained from the contact forces directly given by the numerical simulation. A comparison of the 3 curves on the right and left-hand sides in the corresponding figures shows the influence of the main assumptions. The difference between the plain curve (A) and the dotted curve (C) indicates the error made by neglecting the heterogeneity of the stresses in the sample. The difference between curve (B) and the previous one (C) especially highlights the effects of a possible imperfect relation between the external hoop strain and the internal pressure.

#### 4.4.4 Discussion and validation of the method with the concrete model n°1

The first figures 11 and 12 correspond to the 1D-strain compression tests performed on concrete n°1 assuming zero friction. No difference is observed between A (imposed material behaviour) and B (processing method) (figure 11). This very good agreement proves the quality of the processing method when there is no friction (satisfactory interpolation taking account of the specimen length). On the other hand, the poorer comparisons seen in figure 12 show the effect of neglecting the axial contraction of the sample (figure 12a, definition 17), or its radial swelling, to evaluate the axial stress (figure 12b, definition 18) or neglecting again the radial swelling to compute the volumetric strain (figure 12c, definition 19).

$$\bar{\sigma}_{rr}^S(\epsilon_{\theta\theta}^{ext-cell}) \quad (17)$$

$$\bar{\sigma}_{zz}^S(F_{axial}) \quad (18)$$

$$\bar{\epsilon}_{rr}^S = 0 \quad (19)$$

It would appear essential to take into account the plastic behaviour of the cell despite its thickness. Indeed, with the assumption of purely elastic behaviour, one notes an important error in the analysis of the deviatoric and hydrostatic behaviours when the inner pressure reaches approximately 400 MPa. However, this pressure is largely exceeded in the tests presented later.

#### 4.4.5 Influence of the concrete behaviour on the precision of the analysis

Figure 13 presents the analysis of the numerical simulations for types-2, 3 and 4 concretes. When the compaction of the sample is more important (figures 13a and 13c) the analysis appears even more precise. This is explained by the lower stresses and radial strains in the sample. One can note that the method remains relevant up to an equivalent stress of 1000 MPa (figures 13b and 13c). The final bulk modulus, which is reached for a pressure higher than 1 GPa, is correctly described (figure 13b). These 4 numerical simulations confirm that the method correctly predicts the hydrostatic and deviatoric behaviours of geomaterials for a large range of volumetric strains and hydrostatic pressures. The influence of friction on the quality of the analysis is discussed in the following section.

#### 4.4.6 Influence of the friction on the precision of the analysis

In the calculations leading to figure 14, a coefficient of friction equal to 0.1 was used at the concrete sample/ring interface. The contact between the plug and the sample is assumed to be frictionless. In the first case (figure 14a, concrete n°1), one observes a maximum difference ( $\approx 9\%$ ) between curves A and B which is definitely more important than the case without friction

(figure 11). A significant difference (between 10% and 17%) is also observed between curves A and C. This last comparison shows that the difference does not come from a poor estimation of the radial stress but is rather due to the shear stresses induced by the friction. It is also seen that the volumetric strain (from curves B or C) is underestimated at the end of the loading. Both results are in very good agreement with the evaluation of the effects of the friction made in subsections 4.3.3 (overestimation of the axial stress, equation 7) and 4.3.2 (increase of radial strain). Finally, the observed difference between curves A and B (volumetric strain) is less than about 5%, up to a pressure of 900 MPa (figure 14a).

Surprisingly, for the type-3 concrete, the deviatoric stress given by curve (B) is not over-estimated compared to that calculated from curve (C). Once again, this is explained by the calculations of subsection 4.3.3 (see equations 7 and 8 with  $\sigma_{dev}/P \approx 1$  and  $f = 0.1$ ). Indeed, it is shown that a friction coefficient equal to 0.1 leads to a relative over-estimation of the axial stress close to 10% and to a relative over-estimation of the radial stress close to 4% (figure 6). When the deviatoric stress increases with pressure with a ratio ( $\sigma_{dev}/P$ ) close to one (as it is the case in figure 14b), these two effects compensate very well and the deviation (comparing curve B to curve A) in the analysis disappears in spite of the friction (see equations 9 and 10). It follows that curve (B) is very close to curve (A) (figure 14b).

These calculations with friction ( $f = 0.1$ ) were also performed in the case of type-2 and 4 concrete models (corresponding to 20% compaction for a hydrostatic pressure of 1 GPa). One observes a relative deviation smaller than that obtained with the concrete models 1 and 3 due to a lower radial stress level.

These numerical simulations made it possible to evaluate the quality and the robustness of the proposed processing method for 1D-strain compression tests. It appears necessary to take into

account the plastic strain of the confining cell when the inner pressure exceeds approximately 400 MPa. Moreover, as shown in the numerical simulations of the test, one also needs to take into account the sample shortening and its small radial expansion. Friction has a limited influence when the friction coefficient does not exceed 0.1. To conclude, according to these numerical simulations, the deviation from real values of the deviatoric stress and of the volumetric strain due to the method will remain less than 10% and 5%, respectively. According to the last numerical simulation, the deviation of the deviatoric stress will not exceed a few percent if the deviatoric stress increases with pressure with a ratio ( $\sigma_{dev}/P$ ) close to one. This situation corresponds to the concrete tested, the results of which are presented in the next section.

## 5. Dynamic behaviour of MB50 concrete

Three dynamic 1D-strain compression tests were carried out with MB50 concrete samples (diameter: 30 mm, height: 40 mm) and with the confining cells described above. These samples were loaded with the Split Hopkinson Pressure Bars described in section 3. The method used for the analysis of the test results has been presented in section 4.3. The assumption of negligible friction between the cell and the specimen was especially addressed. The deviatoric behaviour (evolution of the deviatoric stress versus the hydrostatic pressure) and the hydrostatic behaviour (evolution of the hydrostatic pressure versus volumetric strain) are computed. A comparison between the 3 tests will allow for an evaluation of the strain-rate effect.

## 5.1 GENERAL FEATURES

As explained in section 3, SHPB data processing provides forces and displacements at the bar ends. Checks were performed that the input and output forces were close enough to each other to ensure the homogeneity of stress fields in the specimen. Equation 2b shows that the output force is a direct measurement (directly proportional to the strain of the transmitted wave) by contrast with the input force (proportional to the algebraic sum of waves with opposite signs). This input force is therefore more affected by experimental noise. Confidence in the specimen equilibrium having also been obtained by numerical simulations (not reported in the paper), the axial force is, in the following, deduced from the output force only. This is in perfect agreement with the traditional data processing of the SHPB [25]. The nominal axial strain-rate is directly derived from formula 2a. Its evolution versus time basically depends on the stress-strain response of the specimen, as is always the case with the SHPB. Having measured the variation of strain-rate with time, the average strain rate is arbitrarily defined, in what follows, as the mean value between the time corresponding to the maximum strain rate ( $\approx 110 \mu\text{s}$ , figure 15a) and the end of the test ( $\approx 870 \mu\text{s}$ , figure 15a). The strain versus time shown in figure 15a looks monotonic as the result of integration.

The results of three tests are presented corresponding to three axial strain-rates:  $80 \text{ s}^{-1}$ ,  $141 \text{ s}^{-1}$ ,  $221 \text{ s}^{-1}$  (associated with striker speeds of 6.13, 12.5 and 19.23 m/s, respectively)

## 5.2. TEST ANALYSIS (special focus on test n°2)

Note that, in the case of tests n°1 and 3, the same figures as those presented later may be found in

appendix A, with particular comments when needed. A special focus on test n°2 is made. This test corresponds to a 1D-strain compression test carried out at a mean strain rate equal to  $141 \text{ s}^{-1}$ . The velocity of the striker is equal to  $12.5 \text{ m/s}$ . The maximum strain rate reached during the test is equal to  $223 \text{ s}^{-1}$ .

### 5.2.1 Experimental data

The evolution of the hoop strains (figure 15b) shows that the strain level at gauge G2, middle of specimen ( $z = 0$  in figure 1b), is higher than at gauges G1 and G3 ( $z = \pm 3H/8$ ) which is in agreement with calculations made in subsection 4.3 (figure 8).

The maximum hoop strain G2 is equal to  $0.15\%$ . Consequently, the cell does not have a purely elastic behaviour (by contrast with test n°1 – see appendix A). Moreover, the strain recorded by the G5 (axial,  $z = 0$ ) gauge is negative during the first  $100 \mu\text{s}$ . This axial strain evolution ( $\varepsilon_{zz}^{(z=0, ext)}$ ) is in agreement with the simulations done without friction ( $f = 0$ ) that are presented in section 4 (figure 7 for instance). When the shortening of the sample is small, the positive hoop strain due to internal pressure induces a negative axial strain (by the Poisson's ratio effect). The barrelling of the cell which appears later with the shortening of the specimen induces a positive (tension) axial strain.

### 5.2.2 Data processing using the proposed method

Looking at the average stress fields in the sample (figure 15c), two phases are observed. Between  $0$  and  $200 \mu\text{s}$ , the axial stress increases whereas the radial stress remains very low, just as in a

uniaxial compression test. The deviatoric stress is then very close to the axial stress. Between 200 and 800  $\mu\text{s}$ , the deviatoric stress increases slowly. The radial stress reaches 450 MPa at the end of the loading while the hydrostatic pressure exceeds 640 MPa. The axial strain evolves from 0 to -12% (figure 15d) and the inner radial strain remains negligible by comparison with the axial strain ( $|\varepsilon_{rr}^{\text{max}}/\varepsilon_{zz}^{\text{max}}| = 3.4\%$ ). The test is thus proved to be a quasi-1D-strain compression test.

### 5.2.3 Hydrostatic and deviatoric behaviours

The deviatoric and the hydrostatic behaviours of this test are plotted in figure 16. The deviatoric stress shows a change in the response for a pressure of the order of 100 MPa. The hydrostatic behaviour is quasi-linear for a pressure greater than 100 MPa and has an apparent bulk modulus around 6 GPa. Very close values are found in the three tests (figure 17).

The measured hydrostatic and deviatoric behaviours do not show strong differences with those assumed for the KST model (particularly in the case of concrete model n°4 that compares figure 13c with figures 16 and 17). It confirms that the above numerical simulations are realistic.

## **5.3. DISCUSSION**

### 5.3.1 Comparison of the deviatoric and the hydrostatic behaviours obtained for the 3 tests

The results obtained in the 3 tests are very close to each other (figure 17, left hand side). Indeed, the corresponding curves are almost superimposed in the pressure range from 50 to 500 MPa. This suggests that the strain rate has a weak influence on the deviatoric behaviour in the observed

domain.

In the same way, the curves describing the hydrostatic behaviour of the 3 tests are well superimposed in the volumetric strain range from 0 to -11% (figure 17, right hand side). The hydrostatic behaviour also seems weakly influenced by the strain rate in the observed range.

### 5.3.2 Comparison of the results given by test n°2 with those found in the literature

Figure 18 shows a comparison of the results of the 1D-strain test n°2 ( $141 \text{ s}^{-1}$ ) with results found in the literature for the same concrete (MB50): quasi-static 1D-strain tests performed by Gatuingt [21] with a smaller cell (external diameter: 50 mm) allowed the hydrostatic (figure 18, right hand side) and the deviatoric behaviours (figure 18, left hand side) [39] to be obtained. Despite the small variations in properties of MB50 concrete, the purpose of the following comparison is not to elaborate a precise concrete model. It is to reinforce the validation of the test and of the processing method by showing that the results are not in contradiction with other results found in the literature. MB50 concrete was also submitted to quasi-static tri-axial tests [23], the results of which are also plotted in figure 18 (left hand side). During these tests, the specimen was first loaded under a pure hydrostatic pressure and then submitted to an axial loading. Several loading paths are shown in figure 18 (left hand side) ending with the maximum deviatoric stress which is reached. The hydrostatic response to pure hydrostatic loading is shown in figure 18 (right hand side).

The deviatoric behaviours are very similar in the intermediate range of pressure (300 MPa-600 MPa). In this range, the influence of the strain rate and of the loading path appears quite small. For higher pressures, a difference appears: the dynamic test can lead to a higher deviatoric stress (950 MPa, test n°3,  $221 \text{ s}^{-1}$ , figure 17) than that of the triaxial test (550 MPa, figure 18)

performed with the highest pressure of confinement (800 MPa).

When quasi-static and 1-D strain tests are observed together, the hydrostatic behaviour of concrete MB50 appears to be influenced by the loading rate. When quasi-static 1D-strain test and the response under a pure hydrostatic loading are compared, it appears to significantly depend on the loading path.

## Conclusion

The three 1D-strain compression tests show that the deviatoric and hydrostatic behaviours appear almost independent of the strain rate in the (rather narrow) studied range of strain rates (80-221 s<sup>-1</sup>). The deviatoric strength increases monotonically with the hydrostatic pressure to reach 950 MPa under a pressure of 900 MPa (test n°3).

This result is different from that obtained in triaxial quasi-static compression tests on the same concrete (MB50), for which a maximum in the deviatoric resistance of around 550 MPa was observed [23]. This difference can be attributed to a strain-rate effect (4 orders of magnitude between quasi-static and the present tests) or it indicates a possible influence of the loading path on the response.

Considering the hydrostatic behaviour, an almost constant dynamic bulk modulus (around 5 to 6 GPa) was observed with the three 1D-strain compression tests up to a pressure of 900 MPa. This is smaller than that deduced from purely hydrostatic compression tests (9 to 20 GPa in that case) using a tri-axial cell (same concrete) [23] but greater than that obtained with a quasi-static 1D-strain test (3 to 4 GPa in that case). The influence of the strain-rate for equivalent loading paths (1D-strain) appears sizeable. However, the comparison between the two quasi-static tests

underlines once again the importance of the loading path.

New information is provided by the tests presented in this paper. The most important, at the present stage, is the description of a new testing device giving 1D strain loading of geomaterials in the dynamic range and the proposition of a method to efficiently analyse experimental data. This method leads to the knowledge of the deviatoric and hydrostatic behaviours of the material tested. It is shown that the plastic behaviour of the cell as well as the shortening and the swelling of the specimen have to be taken into account in the analysis. The possible influence of a friction coefficient (smaller than 0.1) between the specimen and the cell was investigated by means of numerical simulations of the cell loaded by internal pressure and internal shear stress. Various numerical simulations of the test were carried out with different sets of parameters for the concrete plasticity model of Krieg, Swenson and Taylor. The method was applied successfully to artificial experimental data (free of noise) provided by those simulations. Moreover, two numerical simulations were performed with a constant friction coefficient equal to 0.1. These proved there is a weak influence of friction (between the cell and the sample) on the computed response of the concrete behaviour. This is especially true when the deviatoric resistance monotonically increases with the hydrostatic pressure with a ratio close to one. In addition, two methods of assessing the friction based on the outer strains ratio were also proposed and discussed. These two methods were used in experiments showing the friction coefficient is closer to 0 than to 0.1.

A high level of compaction strain (20%) can be produced with this testing device. It mostly operates in a 1D-strain situation. Stresses up to 1000 MPa, confinement pressures up to 600 MPa and a strain rate range between 100 and 500 s<sup>-1</sup> can be achieved to provide suitable data to evaluate the dynamic behaviour of concrete and other rock-like materials under multiaxial dynamic loadings.

## Appendix A

### TEST N°1 (average strain rate: $80 \text{ s}^{-1}$ )

The striker velocity for this test was  $6.13 \text{ m/s}$ , leading to a maximum strain rate of  $145 \text{ s}^{-1}$  and to an average strain rate of about  $80 \text{ s}^{-1}$ . The external hoop-strains that were recorded on the cell are presented in figure 19b. The maximum hoop strain G2 is  $0.064\%$ . Consequently and according to the numerical simulations presented in subsection 4.3 (figure 4), the behaviour of the cell remains in the elastic domain. The difference between the signals of gauges G1 and G3 could be due to a slight relative global displacement between the specimen and the cell.

The average radial stress in the sample (figure 19c) and its average radial strain (figure 19d) are deduced from the measured hoop strains. The axial stress is deduced from the output force and corrected for the above computed radial strain. It is observed that the loading can be divided into two phases: Between  $0$  and  $200 \mu\text{s}$ , the axial stress increases and the radial stress remains very low, like in a uniaxial compression test. The deviatoric stress is therefore very close to the axial stress. Later, between  $200$  and  $800 \mu\text{s}$ , the deviatoric stress increases slowly. The hydrostatic and deviatoric behaviours corresponding to test n°1 are shown in figure 17 (curve “ $80 \text{ s}^{-1}$ ”).

### TEST N°3 (average strain rate: $221 \text{ s}^{-1}$ )

This test corresponds to a 1D-strain compression test carried out at a mean strain rate equal to

221 s<sup>-1</sup>. The striker velocity was 19.23 m/s. The strain rate reached a maximum value equal to 415 s<sup>-1</sup>. Experimental data are plotted in figures 20a and 20b.

The maximum hoop strain G2 was 0.2%. Consequently, the cell did not have a purely elastic behaviour, according to the numerical simulations presented in the subsection 4.3. According to figure 7 in section 4.3., the negative sign of the axial strain (G5 gauge,  $z = 0$ ) at the beginning of the test indicates that the friction coefficient was closer to 0 than to 0.1. The same conclusion is deduced from the small value of the ratio ( $\varepsilon_{zz}^{(z=0, ext)} / \varepsilon_{\theta\theta}^{(z=0, ext)} < 0.25$ ) observed when the axial strain was equal to 15% ( $t = 600 \mu\text{s}$ ).

It is observed that the loading can again be divided into two phases (figure 20c). Between 0 and 100  $\mu\text{s}$ , the axial stress increases and the radial stress remains very low, as in a uniaxial compression test. Between 100 and 800  $\mu\text{s}$ , the deviatoric stress and the hydrostatic pressure increase up to 1000 MPa and 900 MPa, respectively. The radial stress reaches 570 MPa at the end of the test. The axial strain reaches a maximum value of -19%. The inner radial strain remains very small. Consequently this test was close to a 1D-strain compression test. The hydrostatic and deviatoric behaviours corresponding to test n°3 are shown in figure 17 (curve “221 s<sup>-1</sup>”).

The ratio of the outer hoop strains ( $\varepsilon_{\theta\theta}^{(z=3H/8, ext)} / \varepsilon_{\theta\theta}^{(z=0, ext)}$ , figure 21) was computed from the experimental data shown in figure 20b. It should be emphasised that this ratio remains equal to approximately 0.8 whereas the axial strain is lower than -0.1. This ratio can be compared with that calculated by numerical simulation in the case of a cell subjected to an internal pressure (figure 8, section 4.3). In the case of  $h_{press} = 34 \text{ mm}$ , the computed ratio varied from 0.64 to 0.68, depending on the internal pressure applied. The same ratio varied from 0.58 to 0.62 when an internal shear loading corresponding to a friction coefficient equal to 0.1 was added. The value

found in the experiments (0.8) is closer to the result of the 1st numerical simulation ( $f = 0$ ) than to the result of the second simulation ( $f = 0.1$ ). Thus, as explained in section 4.3, this ratio could be used to compute an estimated value of the friction coefficient. In the present test, it indicates again that the friction coefficient is closer to 0 than to 0.1.

Accepted manuscript

## References

- [1] Burlion, N. Compaction des bétons : éléments de modélisation et caractérisation expérimentale. PhD thesis. ENS Cachan, 1997.
- [2] Burlion N., Pijaudier-Cabot G. and Dahan N. Experimental analysis of compaction of concrete and mortar. *Int. J. Numer. Anal. Meth. Geomec* 2001; 25:467-1486.
- [3] Le Vu O. Etude et modélisation du comportement du béton sous sollicitations de grande amplitude. PhD thesis. Ecole Polytechnique, 1998.
- [4] Lindholm U. S., Yeakley L. M. and Nagy A. The dynamic strength and fracture properties of Dressel basalt. *International Journal of Rock Mechanical Mining Sciences and Geomechanical Abstract* 1974; 11:181-199.
- [5] Christensen R.J., Swansow S. R. and Brown W. S. Split Hopkinson bar test on rock under confining pressure. *Experimental Mechanics* 1972 ; 12:508-541.
- [6] Klepaczko J. R., Gary G. and Barberis P. Behaviour of rock salt in uniaxial compression at medium and high strain rates. *Archives of Mechanics, Warsaw* 1991; pp.499-517.
- [7] Goldsmith W., Polivka M., and Yang T. Dynamic behaviour of concrete, *Experimental Mechanics*, 1966; 6:65-79.
- [8] Gong J.C., Malvern L.E. and Jenkins D.A. Dispersion investigation in the split Hopkinson pressure bar, *Journal of Engineering Material Technology* 1990; 112:309-314.
- [9] Tang T., Malvern L.E. and Jenkins D.A., Rate effects in uniaxial dynamic compression of concrete, *Journal of Engineering Mechanics* 1992; 118:108-124.
- [10] Gary G. and Klepaczko J. R. Essai de compression dynamique sur béton, GRECO Geomaterial scientific report, 1992, pp.105-118.
- [11] Gary G. and Zhao H., Measurements of the dynamic behaviour of concrete under impact loading, In *Chinese Journal Mechanics Press. Proceedings of 2nd ISIE'96. Beijing (China).* 1996. p. 208-213.
- [12] Malvern L.E., Jenkinds D.A., Tang T. and McLure S. Dynamic testing of laterally confined concrete, In: *Micromechanics of failure of quasi brittle materials, Elsevier Applied Science*, 1991, 343-352.
- [13] Bertholf L.D., Karnes J. Two-dimensional analysis of the split Hopkinson pressure bar system, *J. Mech. Phys. Solids* 1975, 23:1-19.
- [14] Davies E.D.H., Hunter S.C. The dynamic compression testing of solids by the method of the split Hopkinson pressure bar. *J. Mech. Phys. Solids* 1963, 11:155-179.
- [15] Malinowski J. Z. and Klepaczko J. R. A unified analytic and numerical approach to specimen behaviour in split Hopkinson pressure bar system, *Int J. Mech. Sci.* 1986; 28: 381-391.
- [16] Gorham, D.A. Specimen inertia in high strain-rate compression. *J.Phys D Appl.Phys* 1989; 22:1888-1893.
- [17] Semblat J.F., Gary G. and Luong M.P., Dynamic response of sand using 3D Hopkinson bar, In: *Proceedings of IS-TOKYO'95 First International Conference on Earthquake Geotechnical Engineering, Tokyo (Japan), 1995.*
- [18] Gary G., Bailly P., Behaviour of a quasi-brittle material at high strain rate. *Experiment and modelling, European Journal of Mechanics* 1998; 17(3):403-420.
- [19] Bragov A.M., Grushevsky G.M. and Lomunov A.K., Use of the Kolsky Method for Studying Shear Resistance of Soils, *Dymat Journal* 1994; 3:253-259.
- [20] Toutlemonde, F. Résistance au choc de structures en béton, PhD thesis, Ecole Nationale des Ponts et Chaussées, 1994.
- [21] Gatuingt, F. Prévision de la rupture des ouvrages en béton sollicités en dynamique rapide, PhD

thesis, ENS Cachan, 1999.

- [22] Gatuingt F. and Pijaudier-Cabot G. Coupled damage and plasticity modelling in transient dynamic analysis of concrete. *Int. J. Numer. Anal. Meth. Geomec.* 2002 ; 26 :1--24.
- [23] Buzaud, E. Performances mécaniques et balistiques du microbéton MB50. DGA/Centre d'Etudes de Gramat report 1998.
- [24] Hopkinson B. A Method of measuring the pressure in the deformation of high explosive by impact of bullets, *Philosophical Transactions of the Royal Society of London* 1914; A213:437-456.
- [25] Kolsky H. An investigation of mechanical properties of materials at very high rates of loading, *Proceedings of the Physical Society London* 1949; B 62:676-700.
- [26] Achenbach, J.D. Wave propagation in elastic solids. Amsterdam. Elsevier Science Publisher. 1993.
- [27] Pochhammer L. Uber die fortpflanzungsgeschwindigkeiten kleiner schwingungen in einem unbergrenzten isotropen kreiszylinder. *J. für die Reine und Angewandte Mathematik* 1876; 81:324-336.
- [28] Chree, C. The equations of an isotropic elastic solid in polar and cylindrical coordinates, their solutions and applications. *Trans. Cambridge Philos. Soc.* 1889; **14**: 250-369.
- [29] Davies R.M. A critical study of the Hopkinson pressure bar. *Phil. Trans. Of the Royal Soc* 1948; A 240:375-457.
- [30] Zhao H. and Gary G. On the use of SHPB technique to determine the dynamic behavior of the materials in the range of small strains, *International Journal of Solids & Structures* 1996; 33:3363-3375.
- [31] Jahsman W.E. Re-examination of the Kolsky Technique for measuring dynamic Material behavior, *J. Appl. Mech*, **38**. (1971): 77-82.
- [32] Tyas A. and Watson A. J. An investigation of frequency domain dispersion correction of pressure signals, *Int.J. Impact Eng.* 2001; 25: 87-101.
- [33] Gary G., Klepaczko J.R. and Zhao H. Corrections for wave dispersion and analysis of small strains with Split Hopkinson Bar, In: *Proceedings of "International Symposium of Impact Engineering"*, Sendai (Japan) 1992, 1:73-78.
- [34] Hibitt H.D., Karlsson B.I., and Sorensen P. Abaqus User's manuel, ABAQUS/IMPLICIT 6.1 2001.
- [35] Forquin P., Arias A., Zaera R. An experimental method of measuring the confined compression strength of geomaterials. *Int. J. Solids and Structures* (Article in Press, Available on line) 2006.
- [36] Krieg R.D. A simple constitutive description for soils and crushable foams. Report, SC-DR-7260883, Sandia National Laboratory 1978.
- [37] Swenson D.V. and Taylor L.M. A finite element model for the analysis of tailored pulse stimulation of boreholes. *Int. J. Num. Analyt. Meth. Geomech.* 1983; 7:469-484.
- [38] Hibitt H.D., Karlsson B.I., and Sorensen P. Abaqus User's manuel, ABAQUS/EXPLICIT 6.1 2001.
- [39] Forquin, P. Endommagement et fissuration de matériaux fragiles sous impact balistique, rôle de la microstructure, PhD Thesis, ENS Cachan, 2003.

Tab. 1. Composition and mechanical properties of MB50 concrete

Composition of MB50 [20]	
Sand (kg/m <sup>3</sup> )	1783
Cement (kg/m <sup>3</sup> )	400
Water (kg/m <sup>3</sup> )	200
Admixture (kg/m <sup>3</sup> )	12
Water/Cement	0.5
Max grain size (mm)	5
Mechanical properties of MB50 [20]	
Compressive strength (MPa)	70
Tensile strength (MPa)	3.0

Tab. 2. Parameters of the Krieg, Swenson and Taylor model used in the numerical simulations

Density, Young's modulus, Poisson's ratio:	$\rho, E, \nu$	2.386, 36 GPa, 0.2
First point of the compaction curve:	$\varepsilon_v^{(1)}, P^{(1)}$	-0.003, 60 MPa
Initial and final bulk moduli:	$K_i, K_f$	20 GPa, 20 GPa
Coefficients of the elliptic equation:	$a_0, a_1, a_2$	1800 MPa <sup>2</sup> , 240 MPa, 0.6
4 sets of parameters used in the numerical simulations (cf. figure 9)		
Concrete n°1:	$\sigma_{mises}^{max}, \varepsilon_v^{(2)}, P^{(2)}$	550 MPa, -0.1, 1 GPa
Concrete n°2:		550 MPa, -0.2, 1 GPa
Concrete n°3:		1000 MPa, -0.1, 1 GPa
Concrete n°4:		1000 MPa, -0.2, 1 GPa

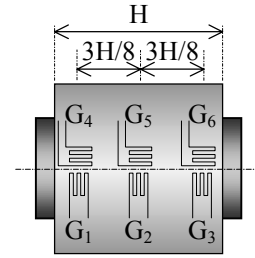
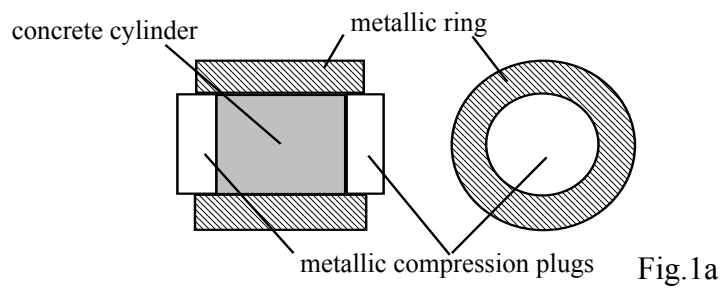


Fig.1. Complete loading cell

Accepted manuscript

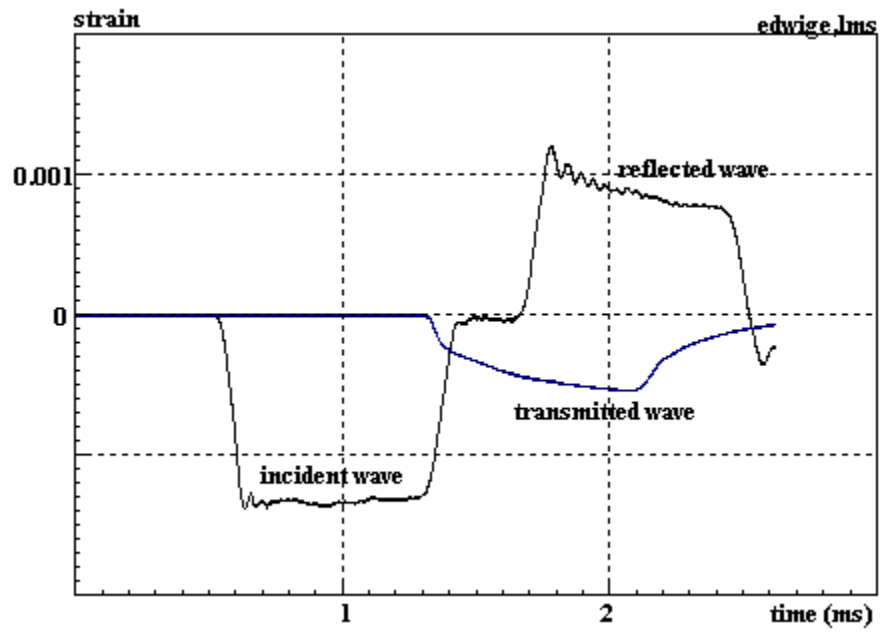


Fig. 2. Basic waves recorded in test n°2 (striker speed: 12.5 m/s).

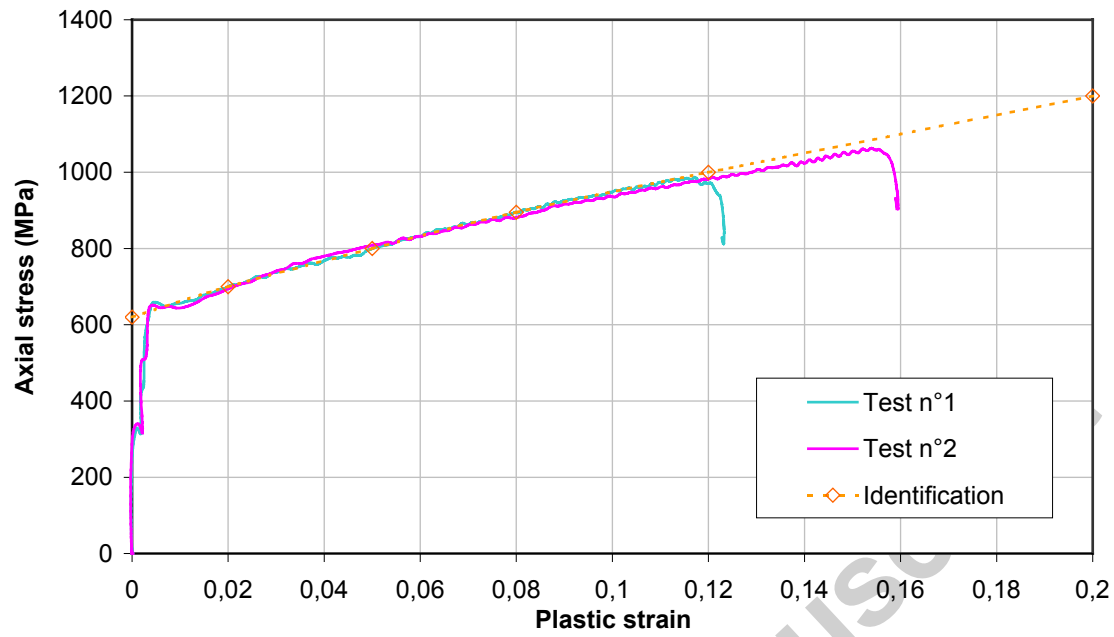


Fig. 3. 1D stress-strain behaviour of the steel of the cell

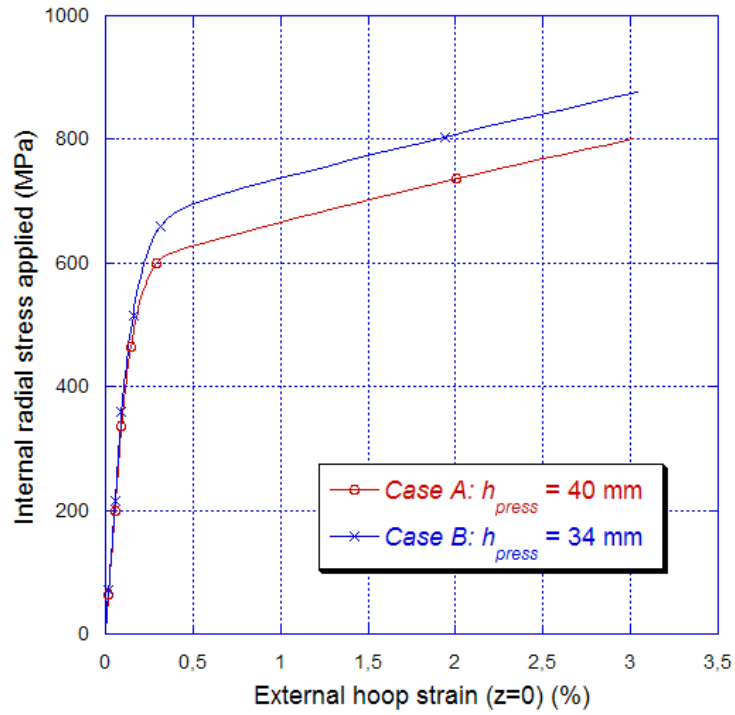


Fig. 4. Internal pressure versus external hoop strain, from the numerical simulation of a cell internally loaded by a pressure applied to its central part (case A: 40 mm, case B: 34 mm)

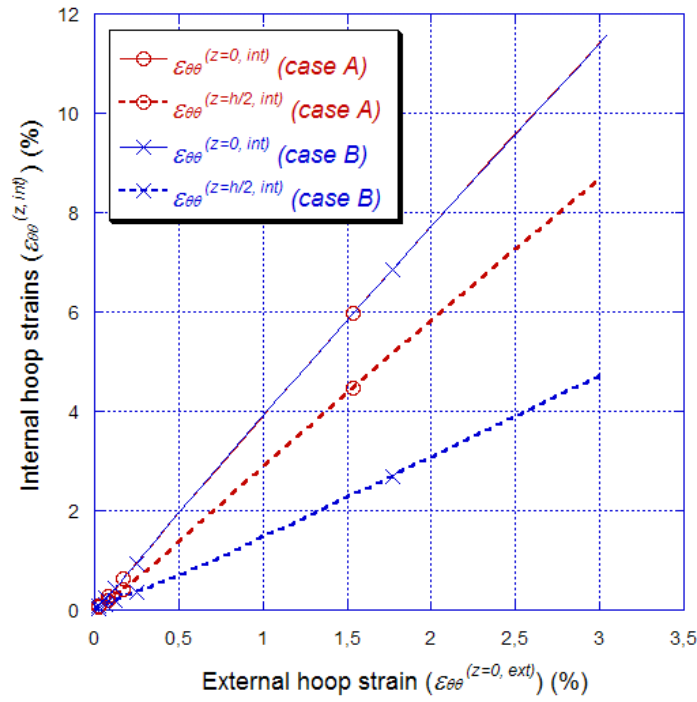


Fig. 5. Internal hoop strains ( $z = 0$  and  $z = h_0/2$ ) versus external hoop strain ( $\varepsilon_{\theta\theta}^{(z=0, ext)}$ ), from the numerical simulation of a cell internally loaded by a pressure applied to its central part (case A: 40 mm, case B: 34 mm)

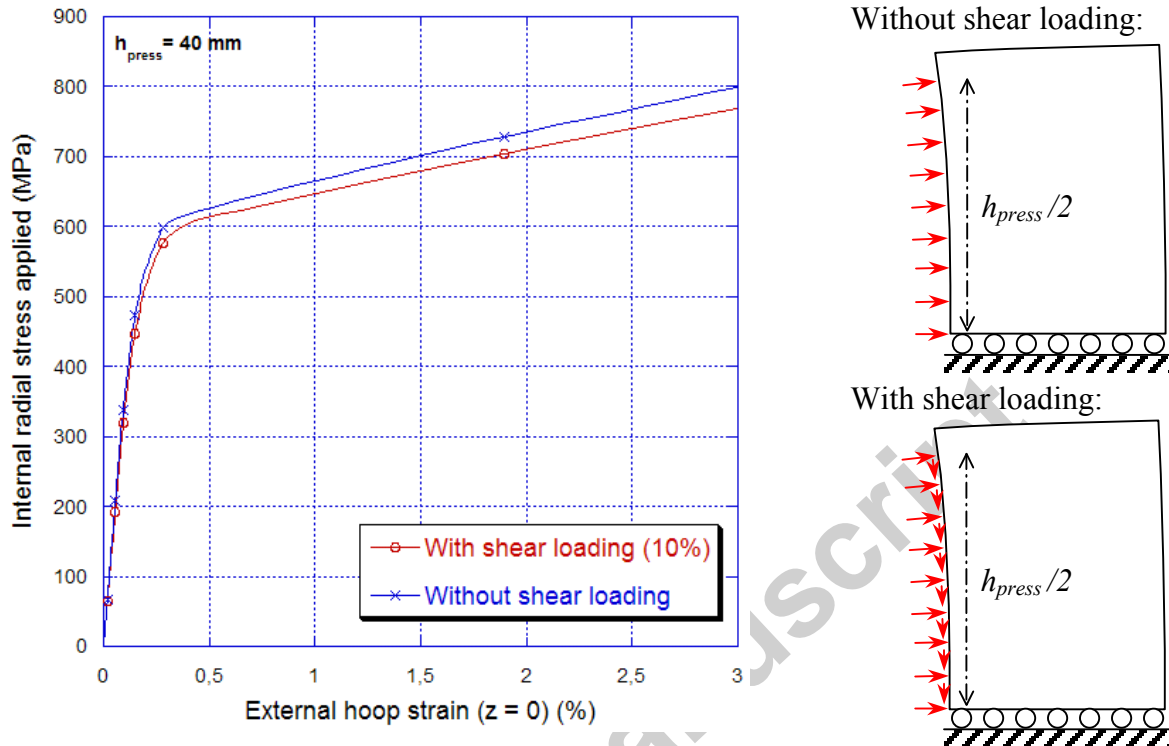


Fig. 6. Numerical simulation of a cell under internal pressure (0-800 MPa) and shear (0-80 MPa) loading. Height of the loaded area: 40 mm

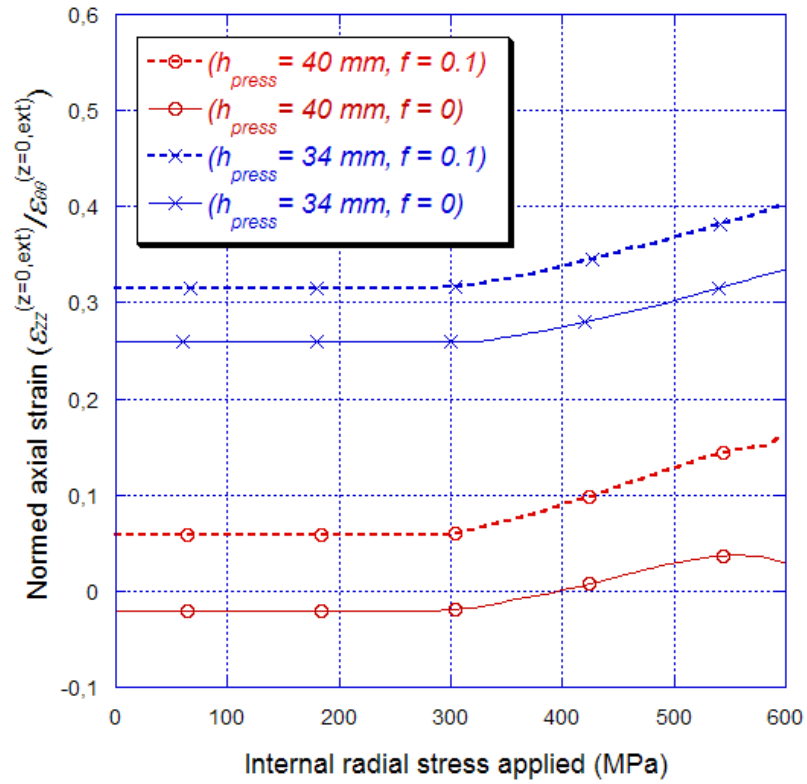


Fig. 7. Ratio of the external axial strain at middle point ( $z = 0$ ) to the hoop strain at the same point

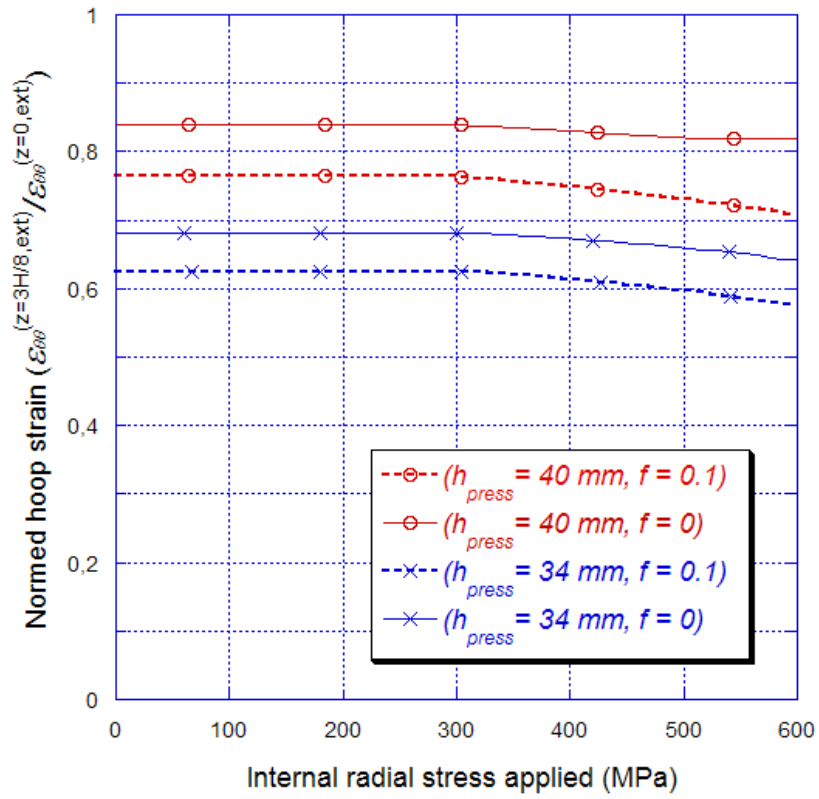


Fig. 8. Ratio of hoop strain at point  $z = 3H/8$  to the hoop strain at middle point ( $z = 0$ )

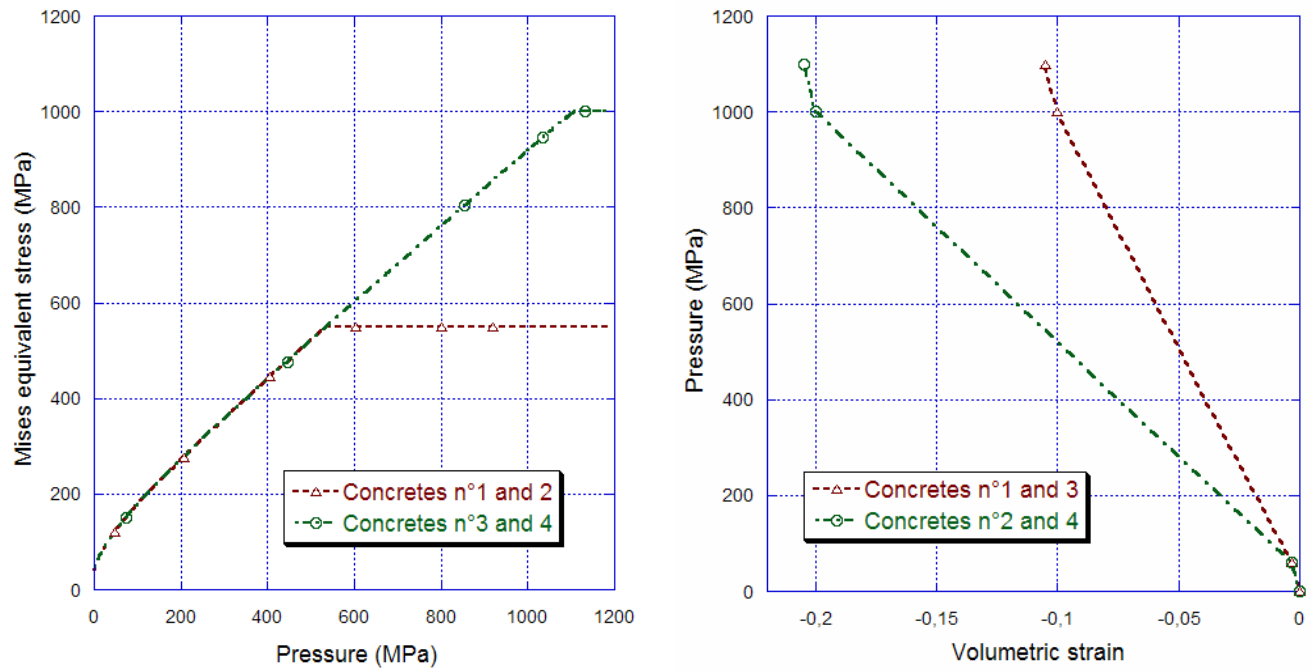


Fig. 9. Behaviour laws used for concretes n°1, 2, 3 and 4 (Left hand side: deviatoric strength versus pressure, Right hand side: pressure versus volumetric strain)

Fig. 10a

Hoop strain  $\varepsilon_{\theta\theta}$ Axial strain  $\varepsilon_{zz}$ 

Fig. 10b

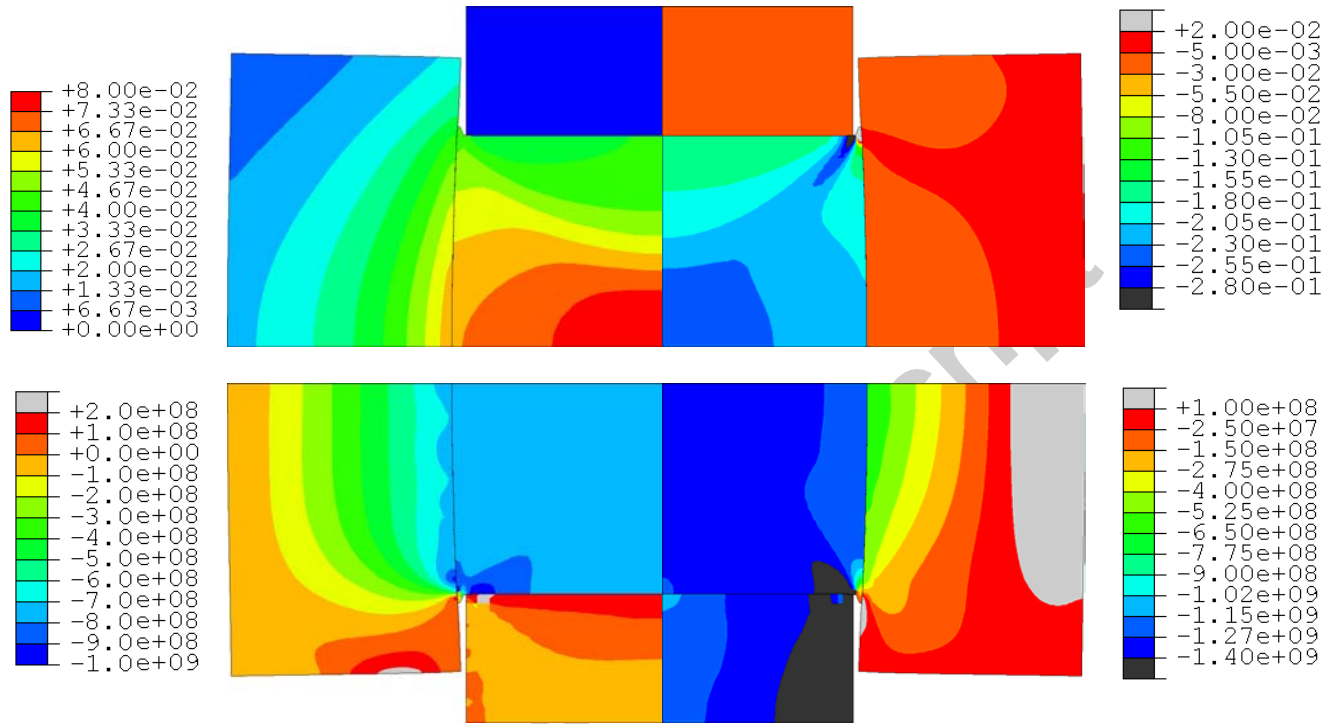


Fig. 10c

Radial stress  $\sigma_{rr}$  (Pa)Axial stress  $\sigma_{zz}$  (Pa)

Fig. 10d

Fig. 10. Main results of the numerical simulation of the test ( $\varepsilon_{\text{axial}} = -20\%$ , concrete n°1, friction coefficient = 0 at contact faces)

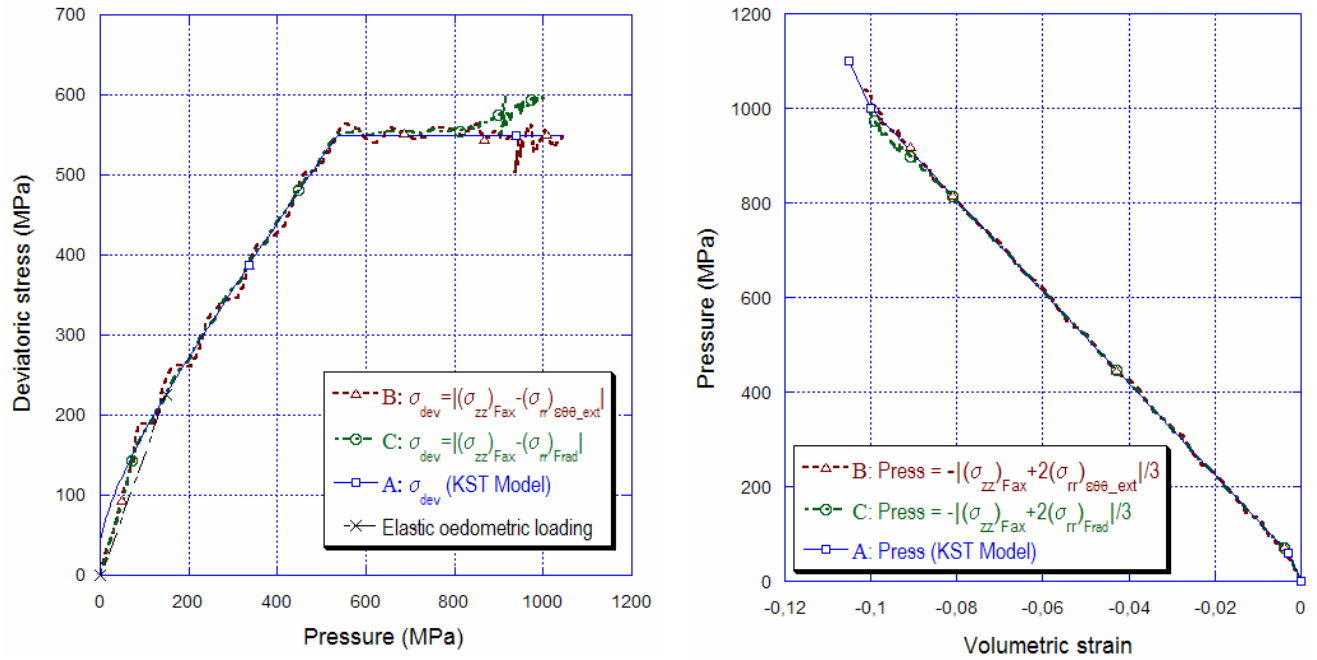


Fig. 11. Results of the numerical simulation of the 1D-strain compression test (no friction between the specimen and the cell, Concrete n°1)

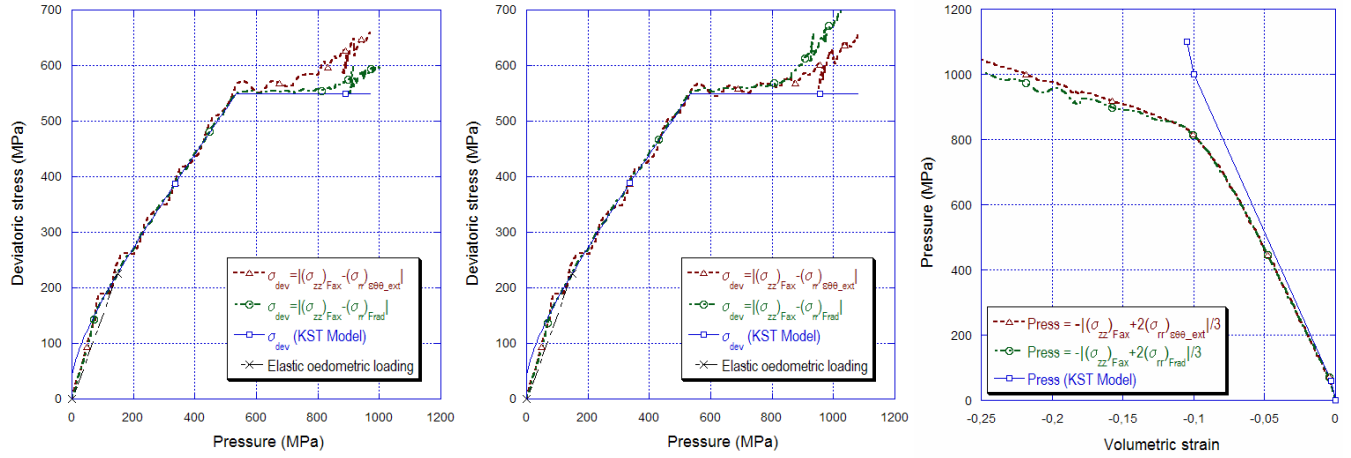


Fig. 12. Illustration of possible uncompleted assumptions used in the processing of experimental data (based on the results of the numerical simulation of the 1D-strain compression test - no friction, concrete model n°1)

Fig. 12a, left. The shortening of the specimen is neglected to compute the radial stress

Fig. 12b, centre. The swelling of the specimen is neglected to compute the axial stress

Fig. 12c, right. The swelling of the specimen is neglected to compute the volumetric strain

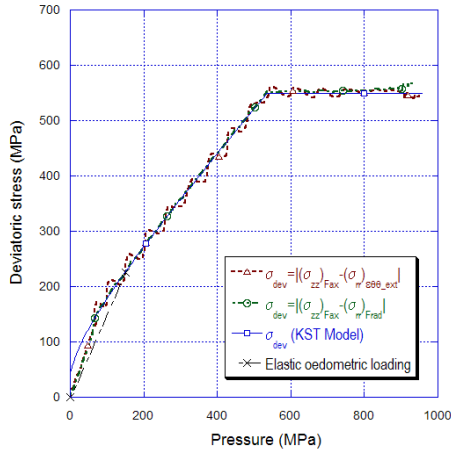


Fig. 13a

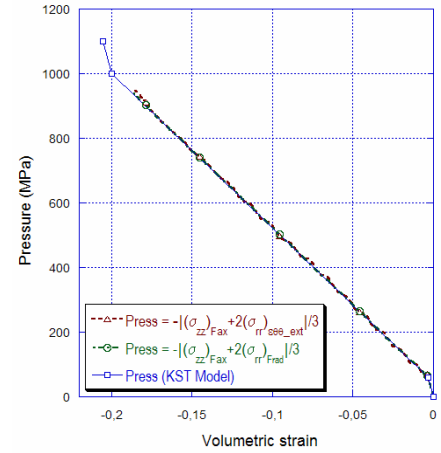


Fig. 13b

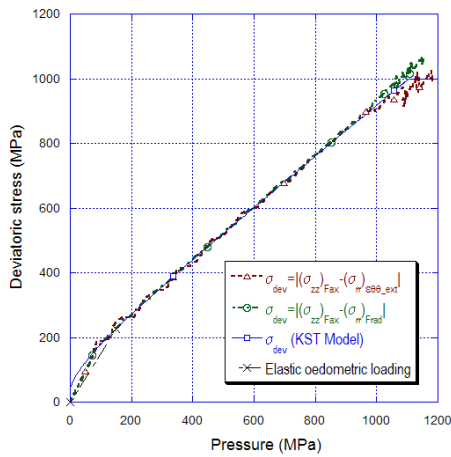


Fig. 13c

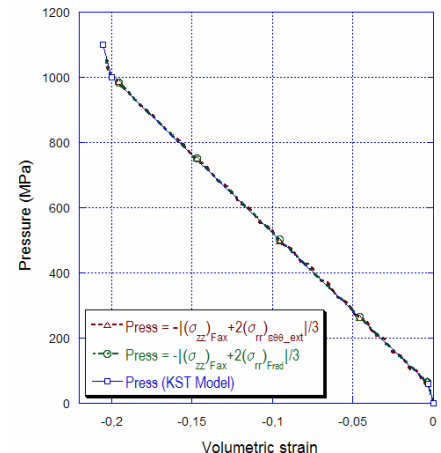
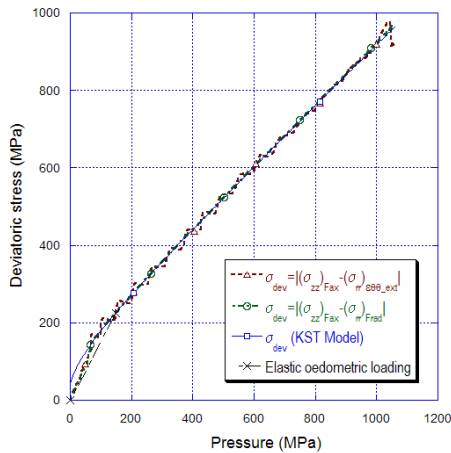
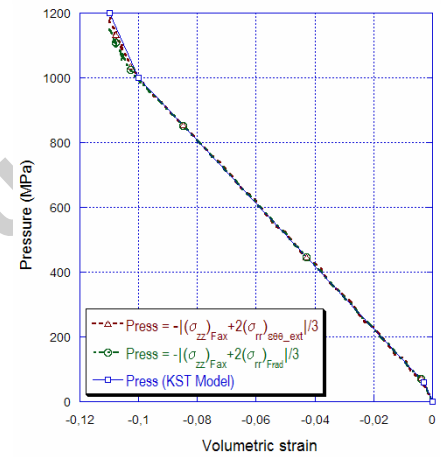


Fig. 13. Results of numerical simulations of 1D-strain compression test

Fig. 13a. Concrete model n°2, no friction between the specimen and the cell

Fig. 13b. Concrete model n°3, no friction between the specimen and the cell

Fig. 13c. Concrete model n°4, no friction between the specimen and the cell

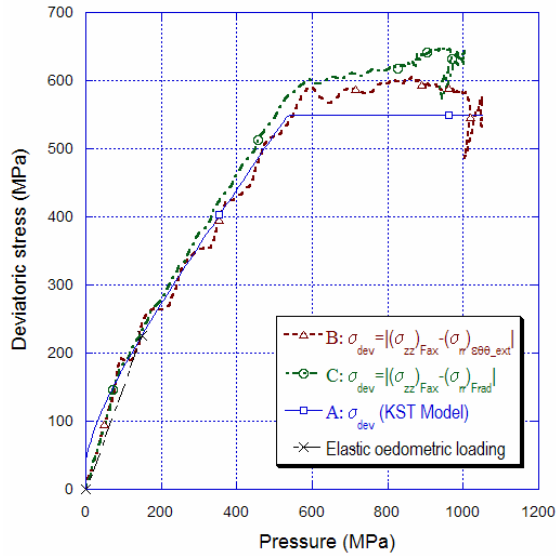


Fig. 14a

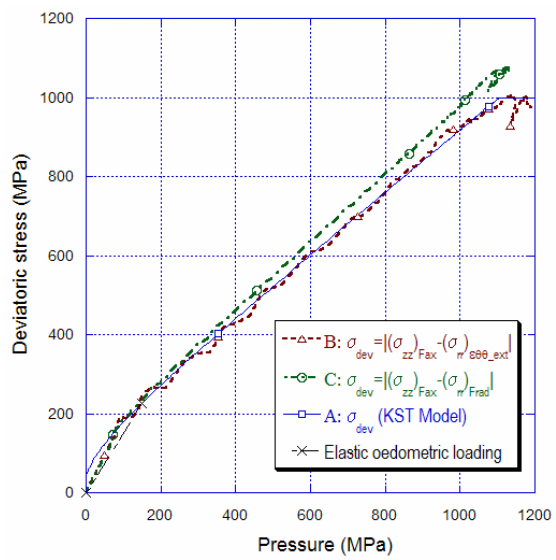
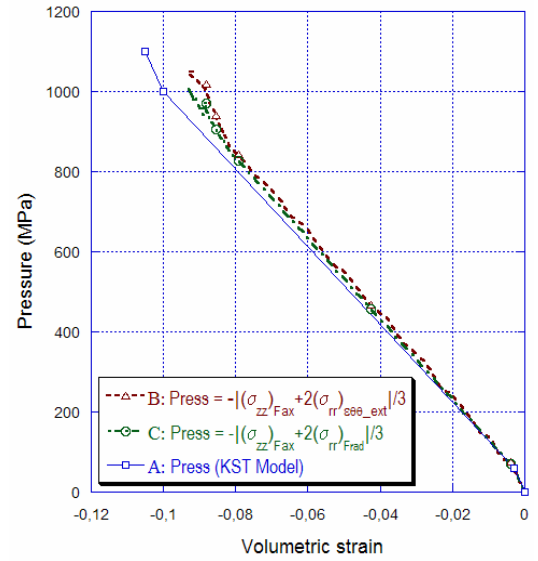


Fig. 14b

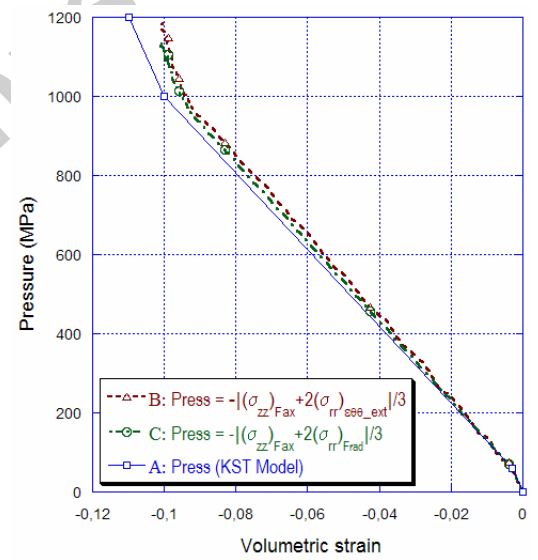


Fig. 14. Results of numerical simulations of 1D-strain compression test

Fig. 14a. Concrete model n°1, friction between the specimen and the cell:  $f = 0.1$

Fig. 14b. Concrete model n°3, friction between the specimen and the cell:  $f = 0.1$

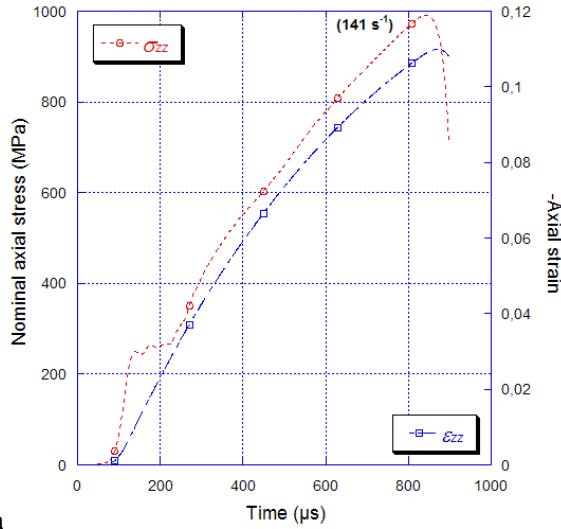


Fig. 15a

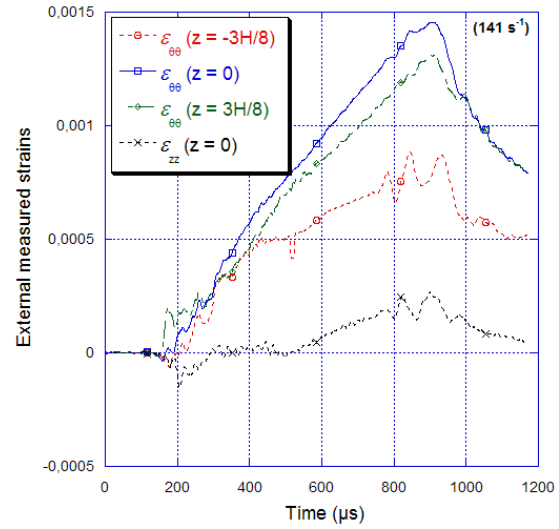


Fig. 15b

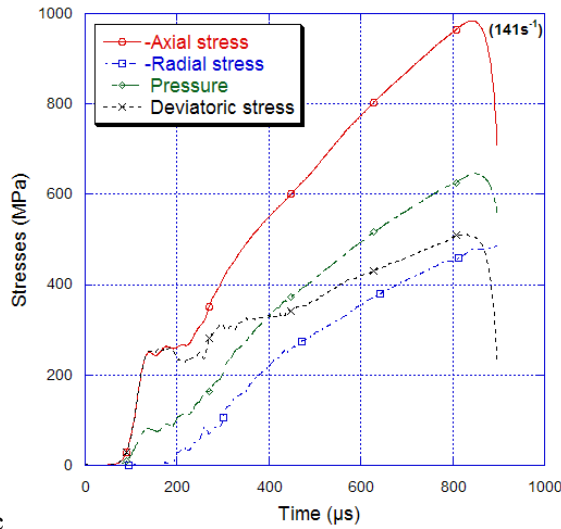


Fig. 15c

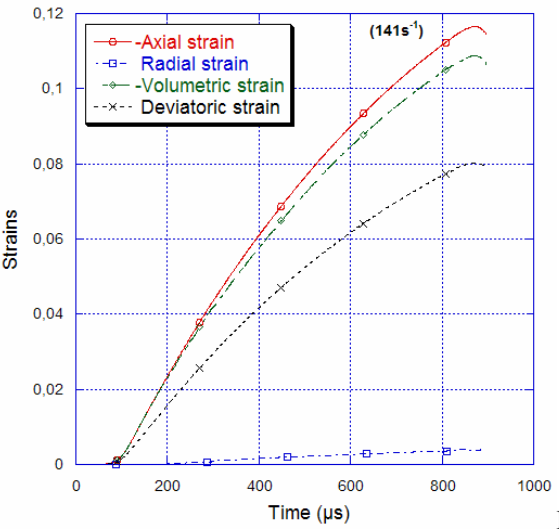


Fig. 15d

Fig. 15. Second dynamic 1D-strain compression test: evolution of stresses and strains with time

Fig. 15a. Nominal axial stress and strain of the specimen versus time (experimental data)

Fig. 15b. Strains measured on the outer surface of the cell ( $\epsilon_{\theta\theta}^{(z=0, ext)}$ ,  $\epsilon_{\theta\theta}^{(z=3H/8, ext)}$ ,  $\epsilon_{\theta\theta}^{(z=-3H/8, ext)}$ ,  $\epsilon_{zz}^{(z=0, ext)}$ ), (experimental data)

Fig. 15c. Average stresses in the specimen (from processed data)

Fig. 15d. Average strains in the specimen (from processed data)

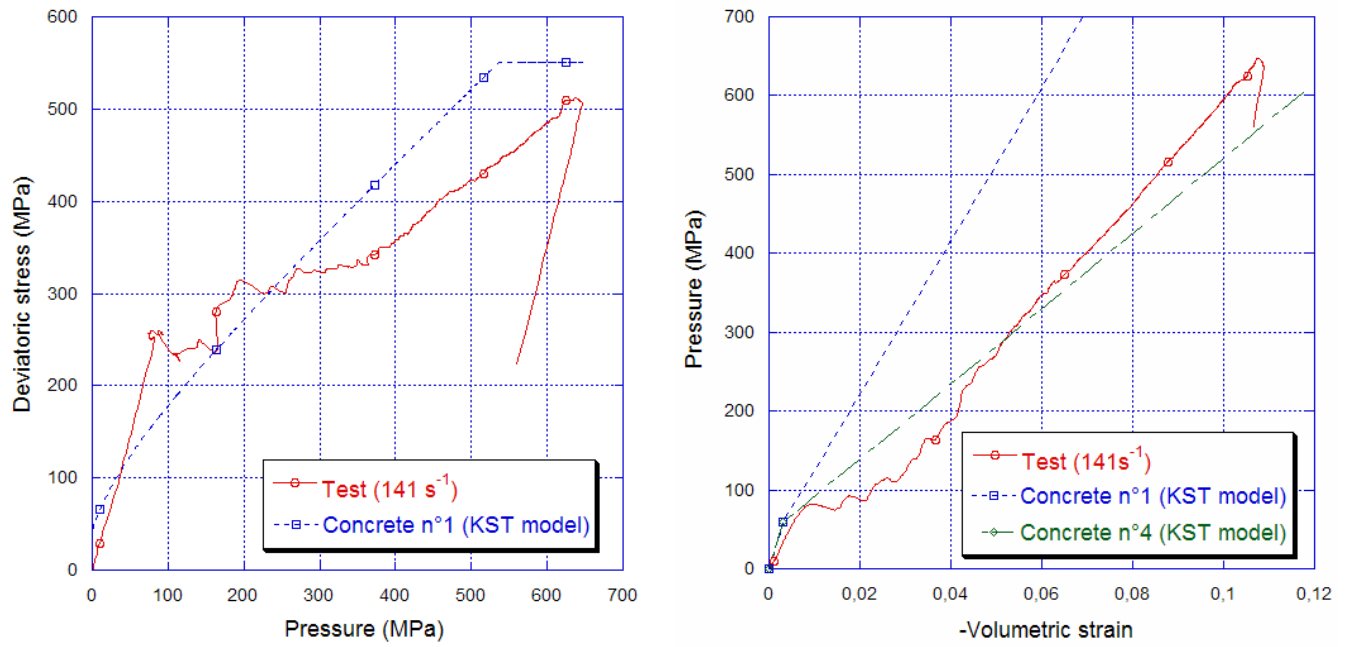


Fig. 16. Behaviours of concrete MB50 at strain rate of  $141 \text{ s}^{-1}$  compared with that of concrete models n°1 and 4

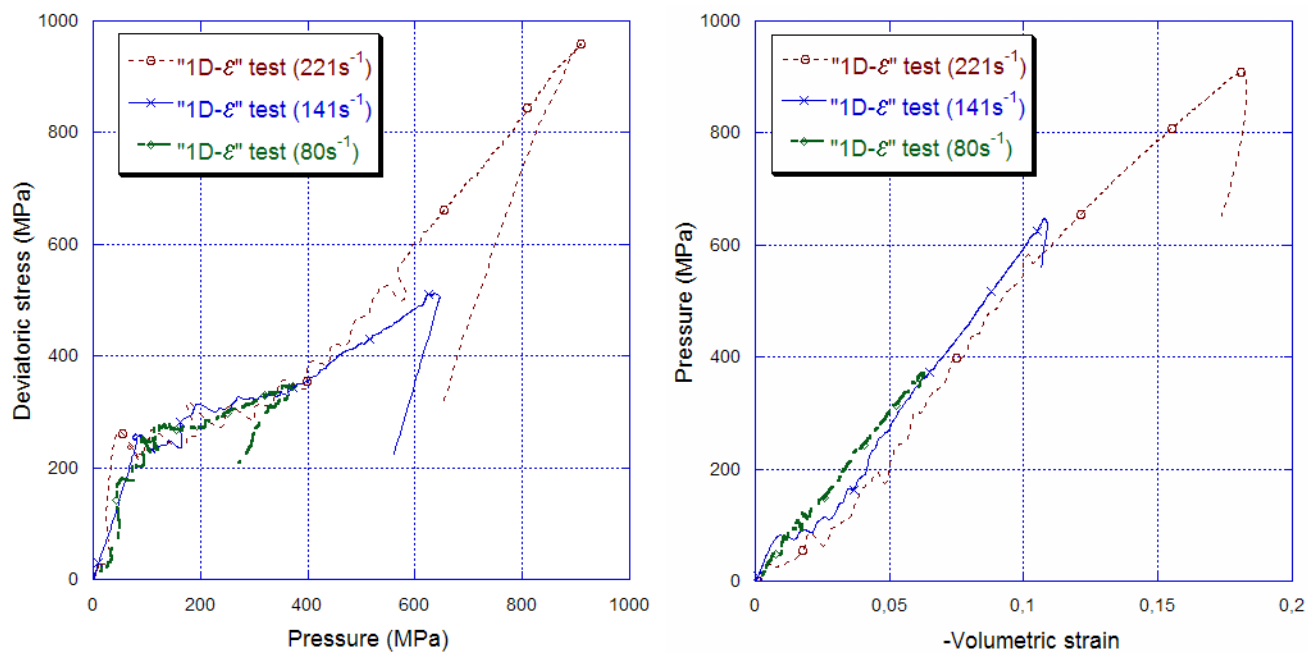


Fig. 17. Comparison of the behaviour deduced from tests 1 to 3

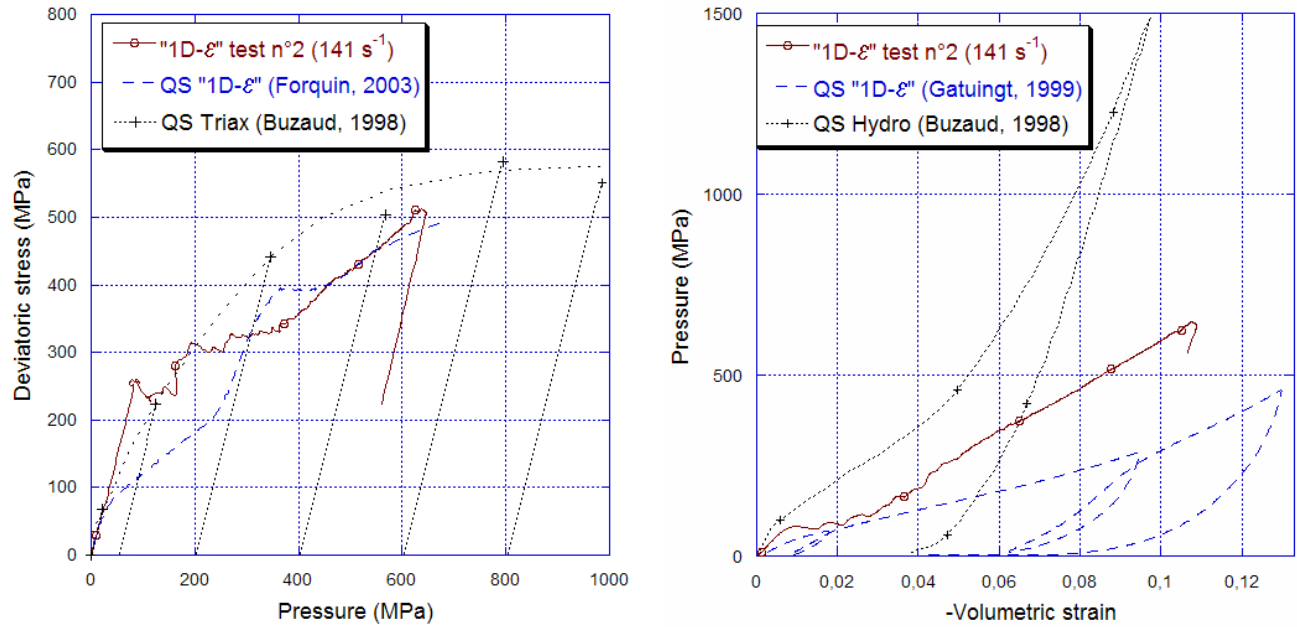


Fig. 18. Comparison of behaviours of concrete MB50 based on measurements made with three different experimental devices: 1D-strain test n°2; Quasi-static 1D-strain tests [21, 39]; Quasi-static triaxial and purely hydrostatic compression tests (from Buzaud [23]).

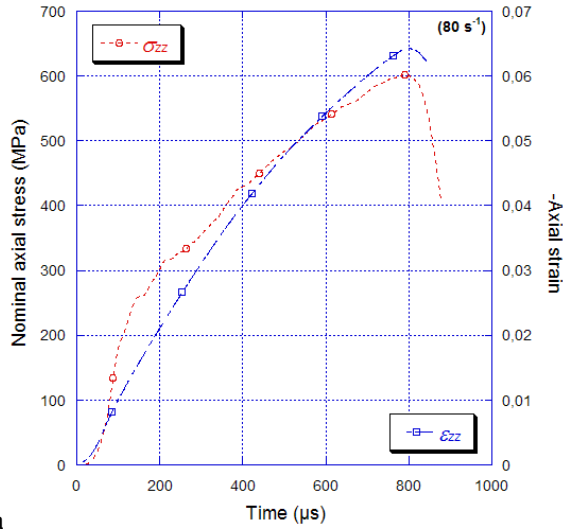


Fig. 19a

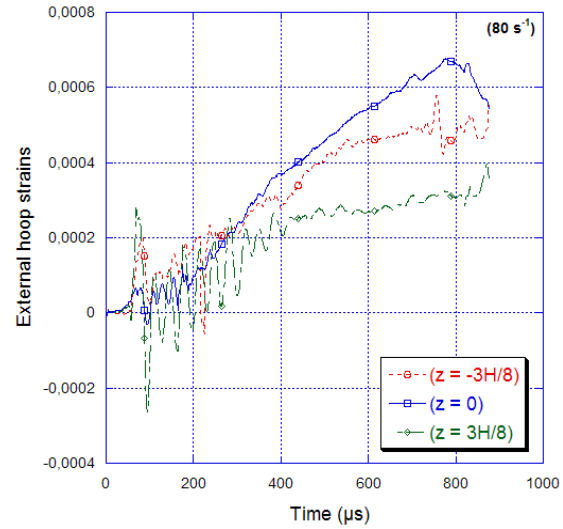


Fig. 19b

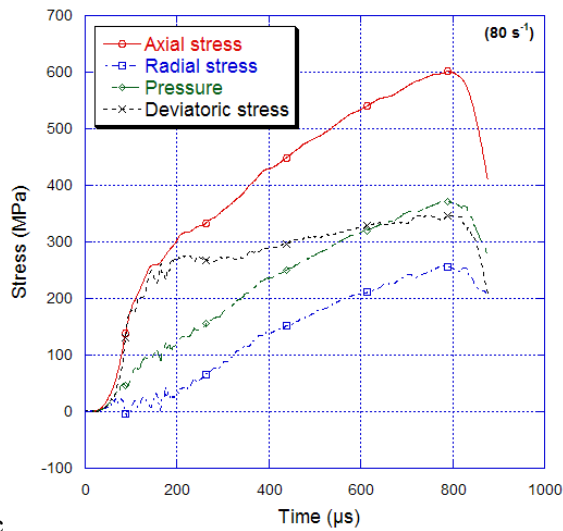


Fig. 19c

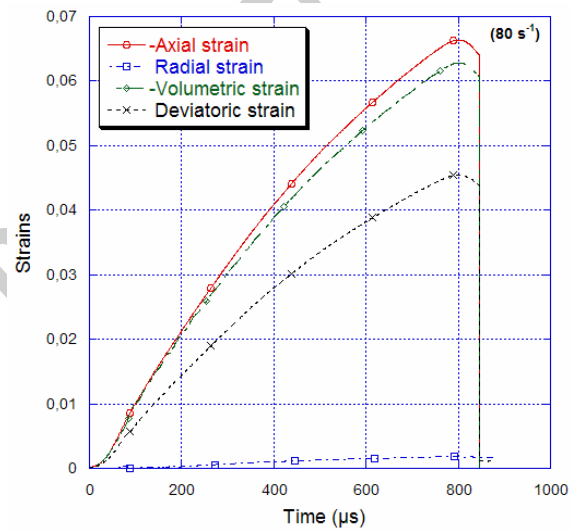


Fig. 19d

Fig. 19. First dynamic 1D-strain compression test: evolution of stresses and strains with time

Fig. 19a. Nominal axial stress and strain of the specimen versus time (experimental data)

Fig. 19b. Strains measured on the outer surface of the cell ( $\epsilon_{\theta\theta}^{(z=0, ext)}$ ,  $\epsilon_{\theta\theta}^{(z=3H/8, ext)}$ ,  $\epsilon_{\theta\theta}^{(z=-3H/8, ext)}$ ), (experimental data)

Fig. 19c. Average stresses in the specimen (from processed data)

Fig. 19d. Average strains in the specimen (from processed data)

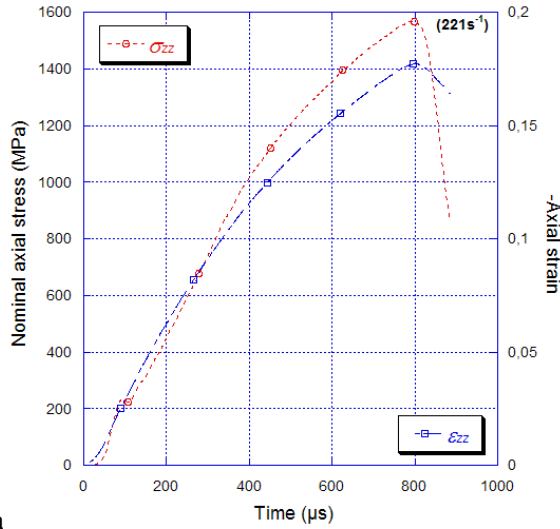


Fig. 20a

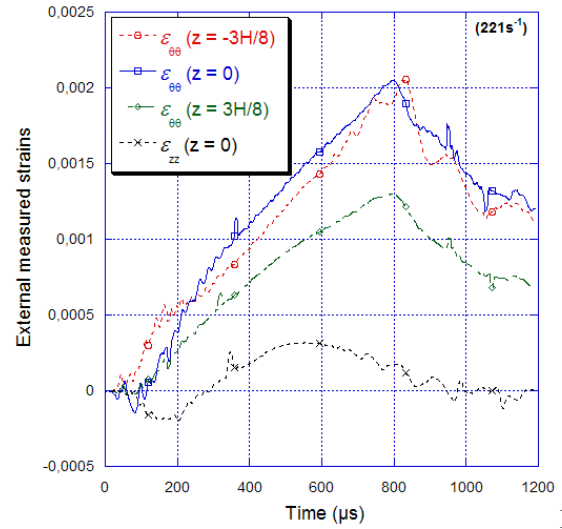


Fig. 20b

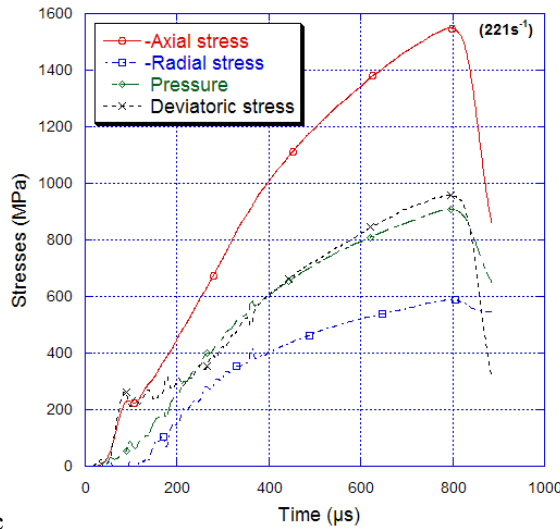


Fig. 20c

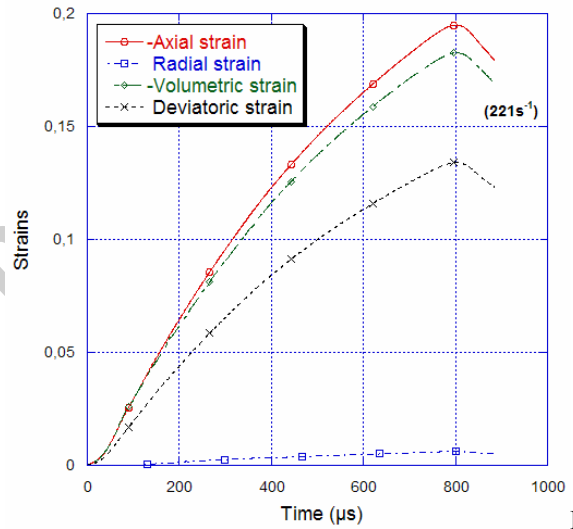


Fig. 20d

Fig. 20. Third dynamic 1D-strain compression test: evolution of stresses and strains

Fig. 20a. Nominal axial stress and strain of the specimen versus time (experimental data)

Fig. 20b. Strains measured on the outer surface of the cell ( $\epsilon_{\theta\theta}^{(z=0, ext)}$ ,  $\epsilon_{\theta\theta}^{(z=3H/8, ext)}$ ,  $\epsilon_{\theta\theta}^{(z=-3H/8, ext)}$ ,  $\epsilon_{zz}^{(z=0, ext)}$ ), (experimental data)

Fig. 20c. Average stresses in the specimen (from processed data)

Fig. 20d. Average strains in the specimen (from processed data)

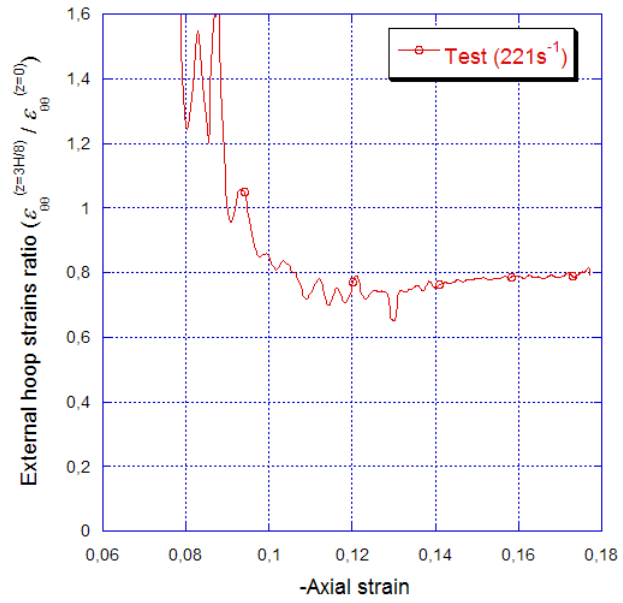


Fig. 21. Ratio of external hoop strains ( $\epsilon_{\theta\theta}^{(z=3H/8, ext)} / \epsilon_{\theta\theta}^{(z=0, ext)}$ )